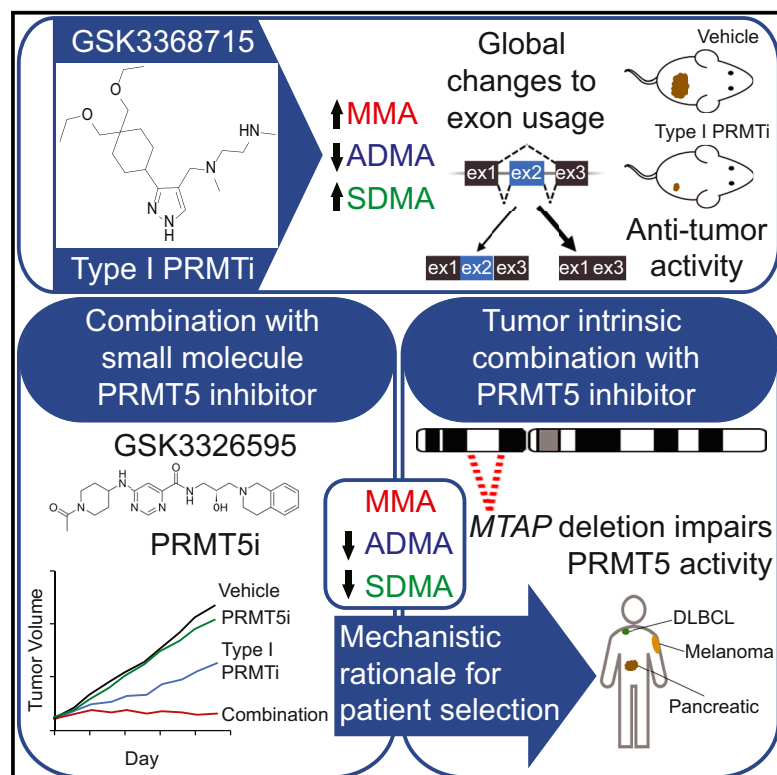


Cancer Cell

Anti-tumor Activity of the Type I PRMT Inhibitor, GSK3368715, Synergizes with PRMT5 Inhibition through MTAP Loss

Graphical Abstract



Authors

Andrew Fedoriw,
 Satyajit R. Rajapurkar,
 Shane O'Brien, ..., Ryan G. Kruger,
 Olena Barbash, Helai P. Mohammad

Correspondence

helai.x.mohammad@gsk.com

In Brief

Fedoriw et al. show that the type I protein arginine methyltransferases (PRMT) inhibitor GSK3368715 has strong anti-cancer activity and synergizes with PRMT5 inhibition. MTAP deficiency causes accumulation of an endogenous PRMT5 inhibitor, suggesting MTAP status as a predictive biomarker for GSK3368715.

Highlights

- GSK3368715 is a potent inhibitor of type I protein arginine methyltransferases
- GSK3368715 alters exon usage and has activity against multiple cancer models
- GSK3368715 synergizes with the PRMT5 inhibitor GSK3326595 to inhibit tumor growth
- *MTAP* gene deficiency impairs PRMT5 activity, sensitizing cancer cells to GSK3368715



Anti-tumor Activity of the Type I PRMT Inhibitor, GSK3368715, Synergizes with PRMT5 Inhibition through MTAP Loss

Andrew Fedoriv,¹ Satyajit R. Rajapurkar,¹ Shane O'Brien,¹ Sarah V. Gerhart,¹ Lorna H. Mitchell,² Nicholas D. Adams,¹ Nathalie Rioux,² Trupti Lingaraj,² Scott A. Ribich,² Melissa B. Pappalardi,¹ Niyant Shah,¹ Jenny Laraio,¹ Yan Liu,¹ Michael Butticello,¹ Chris L. Carpenter,^{1,5} Caretha Creasy,¹ Susan Korenchuk,¹ Michael T. McCabe,¹ Charles F. McHugh,¹ Raman Nagarajan,^{3,6} Craig Wagner,³ Francesca Zappacosta,³ Roland Annan,³ Nestor O. Concha,³ Roberta A. Thomas,⁴ Timothy K. Hart,^{4,5} Jesse J. Smith,² Robert A. Copeland,² Mikel P. Moyer,² John Campbell,² Kim Stickland,² James Mills,² Suzanne Jacques-O'Hagan,² Christina Allain,² Danielle Johnston,² Alejandra Raimondi,² Margaret Porter Scott,² Nigel Waters,² Kerren Swinger,² Ann Boriack-Sjodin,² Tom Riera,² Gideon Shapiro,² Richard Chesworth,² Rabinder K. Prinjha,¹ Ryan G. Kruger,¹ Olena Barbash,¹ and Helai P. Mohammad^{1,7,*}

¹Epigenetics Research Unit, GlaxoSmithKline, Collegeville, PA 19426, USA

²Epizyme, Inc, Cambridge, MA 02139, USA

³Medicinal Science and Technology, GlaxoSmithKline, Collegeville, PA 19426, USA

⁴Nonclinical Safety Assessment, GlaxoSmithKline, Collegeville, PA 19426, USA

⁵Present address: Rubius Therapeutics, Cambridge, MA 02139, USA

⁶Present address: Genomic Variation Laboratory, UC Davis, Davis, CA 95616, USA

⁷Lead Contact

*Correspondence: helai.x.mohammad@gsk.com

<https://doi.org/10.1016/j.ccell.2019.05.014>

SUMMARY

Type I protein arginine methyltransferases (PRMTs) catalyze asymmetric dimethylation of arginines on proteins. Type I PRMTs and their substrates have been implicated in human cancers, suggesting inhibition of type I PRMTs may offer a therapeutic approach for oncology. The current report describes GSK3368715 (EPZ019997), a potent, reversible type I PRMT inhibitor with anti-tumor effects in human cancer models. Inhibition of PRMT5, the predominant type II PRMT, produces synergistic cancer cell growth inhibition when combined with GSK3368715. Interestingly, deletion of the methylthioadenosine phosphorylase gene (*MTAP*) results in accumulation of the metabolite 2-methylthioadenosine, an endogenous inhibitor of PRMT5, and correlates with sensitivity to GSK3368715 in cell lines. These data provide rationale to explore *MTAP* status as a biomarker strategy for patient selection.

INTRODUCTION

Methylation of protein arginine residues regulates a diverse range of cellular processes including transcription, RNA processing, DNA damage response, and signal transduction. In mammalian cells, methylated arginine exists in three major forms: ω - N^G -monomethyl-arginine (MMA), ω - N^G,N^G -asymmetric dimethyl arginine (ADMA), or ω - N^G,N^G -symmetric

dimethyl arginine (SDMA). Each methylation state can affect protein-protein interactions in different ways and, therefore, has the potential to confer distinct functional consequences for the biological activity of the substrate (Yang and Bedford, 2013). Protein arginine methyltransferases (PRMTs) are enzymes that transfer a methyl group from S-adenosyl-L-methionine (SAM) to the substrate arginine side chain, and can be categorized into subtypes based on the final product of the enzymatic reaction (Bedford

Significance

The *MTAP* gene is frequently deleted in human cancers, including tumor types with limited therapeutic options. Although *MTAP* deficiency has been reported to sensitize cells to knockdown of PRMT5, the major catalyst of symmetric arginine methylation, current PRMT5 inhibitors in clinical trials cannot recapitulate this effect due to their mode of inhibition. Combination of PRMT5 inhibitors with GSK3368715, an inhibitor of type I PRMTs, reveals robust synergistic anti-proliferative effects and attenuation of all forms of arginine methylation, providing the mechanistic rationale for the enhanced activity of GSK3368715 observed in *MTAP*-deficient cancer cell lines. The safety and efficacy of GSK3368715, together with the utility of *MTAP* status as a patient selection biomarker, are currently under clinical investigation (NCT03666988).

and Clarke, 2009). All PRMTs can generate MMA through a single methylation event, whereas type I and II enzymes catalyze progression from MMA to ADMA and SDMA, respectively. Among the type I enzymes, the activity of PRMT1 accounts for approximately 85% of cellular ADMA levels (Bedford and Clarke, 2009; Dhar et al., 2013; Pawlak et al., 2000). In many instances, the PRMT1-dependent ADMA modification is required for the biological activity and subcellular trafficking of its substrates (Nicholson et al., 2009).

Overexpression of type I PRMTs have been described in numerous solid and hematopoietic cancers. In several tumor types, this overexpression has been correlated with patient outcome (Altan et al., 2015; Elakoum et al., 2014; Yang and Bedford, 2013; Yoshimatsu et al., 2011). Moreover, experimental evidence suggests that type I PRMTs can contribute to transformation, proliferation, invasiveness, and survival of cancer cells, through methylation of arginine residues found on histone and non-histone substrates that underlie these processes (Almeida-Rios et al., 2016; Cheung et al., 2007; Greenblatt et al., 2016, 2018; Shia et al., 2012; Takai et al., 2014; Veland et al., 2017; Wang et al., 2014; Wei et al., 2014; Yang and Bedford, 2013; Zhao et al., 2008). Overall, disruption of the ADMA modification on key substrates decreases the proliferative capacity of cancer cells (Cheung et al., 2007; Yang and Bedford, 2013), suggesting that inhibition of type I PRMTs may provide an effective strategy for therapeutic intervention in many types of human cancers.

In addition to type I PRMTs, other PRMTs, including the major catalyst of SDMA, PRMT5, have been implicated in cancer biology. This has led to multiple drug discovery efforts by several groups (Chan-Penebre et al., 2015; Shailesh et al., 2018; Smil et al., 2015; Stopa et al., 2015). Successful examples include the recent discovery and characterization of selective PRMT5 inhibitors (GSK3203591 or GSK3326595) (Chan-Penebre et al., 2015; Gerhart et al., 2018) that demonstrate *in vitro* and *in vivo* potency in lymphoma models. Since the publication of these reports, more recent studies have further suggested that PRMT5 activity can also be inhibited by the metabolite 2-methylthioadenosine (MTA), a natural by-product of polyamine synthesis (Kryukov et al., 2016; Marjon et al., 2016; Mavrakis et al., 2016). This inhibition of PRMT5 manifests in a subset of cancers through somatic loss of the gene responsible for MTA metabolism, methylthioadenosine phosphorylase (*MTAP*). Deletion of *MTAP* results in the accumulation of MTA in tumors which, in turn, correlates with decreased SDMA, suggesting that a pre-existing state of attenuated PRMT5 activity can serve as a vulnerability to multiple targets (Kryukov et al., 2016; Marjon et al., 2016; Mavrakis et al., 2016).

Here we describe the discovery and characterization of GSK3368715 (EPZ019997), a potent, reversible type I PRMT inhibitor.

RESULTS

Discovery, Biochemical Characterization, and Cellular Activity of Type I PRMT Inhibitors

Inhibitors of PRMT1 were identified from Epizyme's protein methyltransferase biased compound collection that was designed to identify inhibitors of both lysine methyltransferases

(KMT) and arginine methyltransferases. Following a number of iterative design cycles focused on balancing cellular potency and pharmacokinetic (PK) properties, GSK3368715 and structurally related GSK3368712 were developed as potent inhibitors of PRMT1 (Figures 1A and 1B; Table S1). Detailed biochemical characterization revealed that GSK3368715 and GSK3368712 are potent, reversible inhibitors of the entire type I PRMT family (PRMT1, 3, 4, 6, and 8, K_i^{*app} values ranging from 1.5 to 81 nM for GSK3368715) with minimal inhibition against a panel of lysine methyltransferases, and no inhibition against type II and type III PRMTs (Figure S1A; Table S1). GSK3368715 displays time-dependent inhibition of all the type I PRMTs except PRMT3 (Figure S1B). Enzymatic mode of inhibition studies suggest that GSK3368715 is a SAM uncompetitive, peptide mixed inhibitor of PRMT1 (Figures S1C and S1D). Whereas, kinetically, GSK3368715 seems mixed relative to peptide substrate, the crystal structure of PRMT1 in complex with GSK3368715 demonstrates that GSK3368715 binds in the peptide site directly adjacent to the SAM pocket (Figure 1C; Table S2). This apparent discrepancy may be because time-dependent inhibition is known to artificially mask competitive behavior in these types of experiments.

Knockout (KO) of *Prmt1* in mice results in a decrease of ADMA on cellular proteins, together with increases in MMA and SDMA (Dhar et al., 2013). To investigate the biological effect of type I PRMT inhibition, ADMA, SDMA, and MMA were evaluated in a panel of cancer cell lines treated with GSK3368715 (Figures 1D and S1E–S1G). Decreases in global ADMA levels were evident after the first day of treatment, and maximal by 72 h. Robust MMA and SDMA induction were observed within the first 24 h, and both reached maximal levels after 48 h. The dose response associated with MMA induction revealed a cellular half maximal effective concentration for GSK3368715 of 13.6 ± 0.3 nM (Figure S1H). Collectively, these time- and dose-dependent global changes in arginine methylation demonstrate that GSK3368715 is a potent and cell active inhibitor of type I PRMT activity.

Anti-tumor Activity of GSK3368715

To determine whether the growth and viability of cancer cells may be susceptible to inhibition of type I PRMT activity, the anti-proliferative activity of GSK3368715 was tested in a 6-day proliferation assay across 249 cancer cell lines, representing 12 tumor types. The majority of the cell lines assessed in this panel showed 50% or more growth inhibition by GSK3368715 relative to DMSO-treated cells, as quantified by their growth half maximal inhibitory concentration (GI_{50}) (Figure 2A). Cell death or cytotoxicity was assessed by quantifying the number of cells remaining after treatment relative to the number present at the time of compound addition and the DMSO control at day 6 (growth death index [GDI]). Negative GDI values, indicative of cytotoxic responses, were most pronounced among lymphoma and AML cell lines, with cytotoxicity observed in 56% and 50% of cell lines tested, respectively (Figure 2B). Although the majority of solid tumor cell lines had cytostatic responses to GSK3368715, cytotoxic effects were evident in a subset of these cell lines, including 17% of non-small-cell lung cancer and 13% of pancreatic cancer. Consistent with their comparable biochemical activity and selectivity, GSK3368715

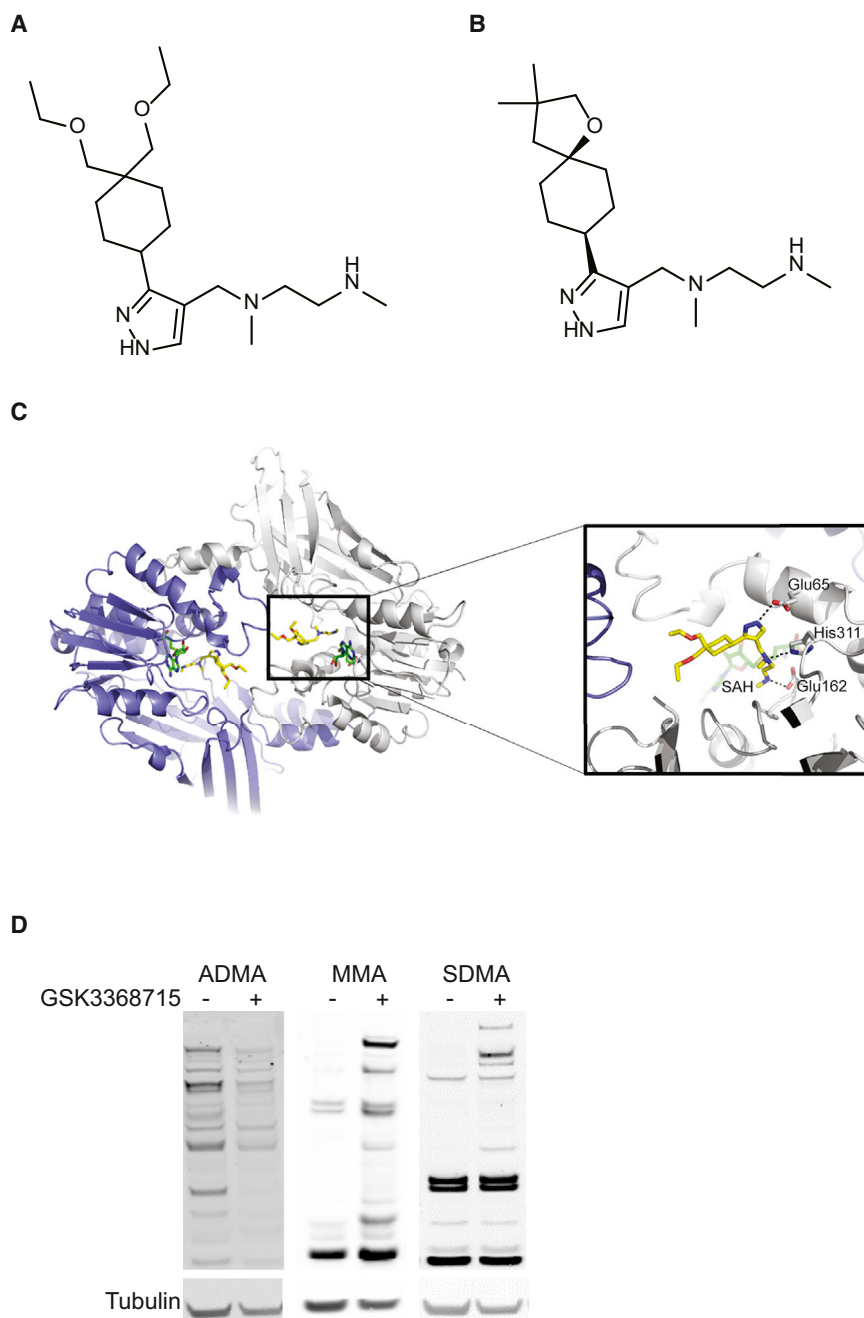


Figure 1. Inhibition of Type I PRMT Activity by GSK3368715

(A and B) Structures of GSK3368715 (A) and GSK3368712 (B).

(C) A ternary complex of PRMT1 with GSK3368715 (orange) and SAH (purple) resolved to 2.48 Å.

(D) Representative western blot of ADMA, MMA, and SDMA changes induced by 2 μM GSK3368715 in the Toledo cell line. See also Figure S1 and Tables S1 and S2.

assay utilizing patient-derived DLBCL models. Type I PRMT inhibition demonstrated anti-proliferative effects in these primary patient samples, achieving 50% or greater growth inhibition at 1.25 μM in 6/10 patient samples and ≥80% growth inhibition in all samples at 5 μM (Figure S2E).

Pharmacokinetic analysis of GSK 3368715 and GSK3368712 revealed that both compounds had suitable PK properties for oral administration and *in vivo* assessment of anti-tumor activity (Table S3). In toxicology studies conducted in rats and dogs, primary on-target toxicity affected the gastrointestinal tract and mild-to-moderate changes to hematopoietic lineages (Table S4), while doses used in mice were well tolerated. The efficacy of type I PRMTi in mice bearing xenografts of cell lines that had cytotoxic responses was examined. The Toledo DLBCL cell line has a cytotoxic response to GSK3368715 with a GI_{50} of 59 nM *in vitro* (Figure 2C). Once-daily administration of GSK3368715 induced dose-dependent inhibition of Toledo tumor growth, with tumor regression in mice treated with >75 mg/kg (Figure 2D). The BxPC3 pancreatic adenocarcinoma cell line has a GI_{50} of 2,100 nM, and was cytotoxic at concentrations above 10 μM GSK3368715 (Figure 2E). Once-daily administration of type I PRMTi had significant effects on the growth of

and GSK3368712 demonstrated equivalent anti-proliferative activity against all cancer cell lines tested and were, therefore, used interchangeably in subsequent studies (Figures S2A and S2B; both subsequently referred to as “type I PRMTi”). To confirm the proliferation screening results, cell-cycle analysis was performed in cytostatic and cytotoxic diffuse large B cell lymphoma (DLBCL) cell lines. Consistent with its negative GDI value, type I PRMTi induced time- and dose-dependent accumulation of cells in sub- G_1 (Figure S2C). In contrast, accumulation of sub- G_1 cells was only detected in the cytostatic OCI-Ly1 line at the highest concentration of type I PRMTi (Figure S2D). The growth inhibitory activity of GSK3368715 was further explored in a colony-forming

BxPC3 xenografts at all doses tested, reducing tumor growth by 78% and 97% in the 150- and 300-mg/kg dose groups, respectively (Figure 2F). Efficacy studies with once-daily administration of 150 mg/kg GSK3368715 in cell line xenograft models of clear cell renal carcinoma (ACHN) and triple-negative breast cancer (MDA-MB-468) revealed tumor growth inhibition of 98% and 85%, respectively (Figures S2F and S2G). In a patient-derived xenograft model of pancreatic adenocarcinoma, type I PRMTi had significant effects on tumor growth, with inhibition >90% in a subset of animals within the 300-mg/kg cohort (Figure 2G). These data demonstrate that GSK3368715 has potent, anti-proliferative activity across cell lines representing a

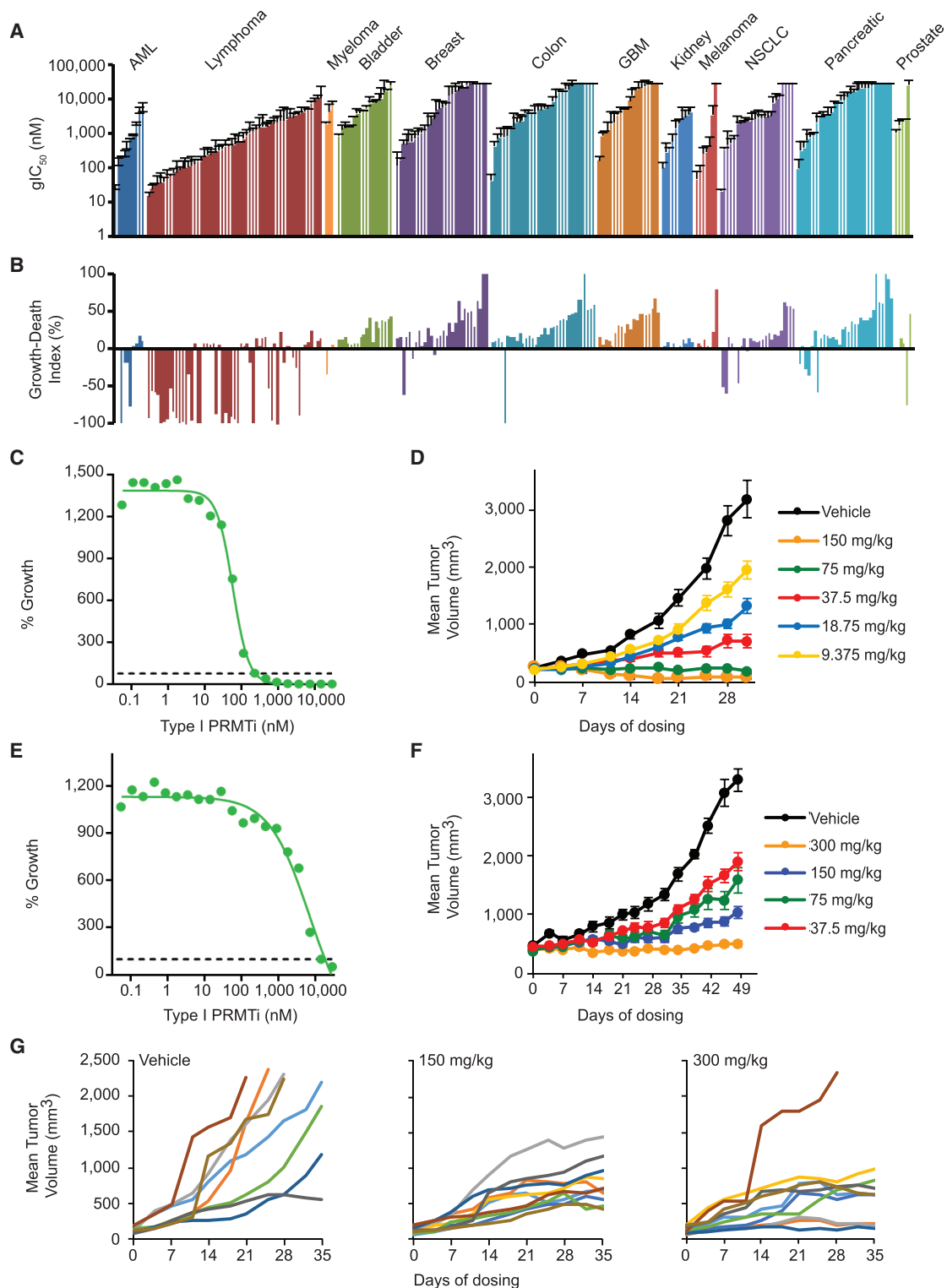


Figure 2. Anti-proliferative Activity of GSK3368715

(A and B) Growth IC₅₀ (A) and growth death index (B) values from a 6-day proliferation assay with GSK3368715 in 249 cancer cell lines ($n \geq 2$ experiments per cell line; mean \pm SEM).

(C and D) *In vitro* dose-response curve (C) and average tumor volumes of mice treated once daily with type I PRMTi (GSK3368715) (D) for the Toledo cell line. For (D), $n = 10$ animals per group and error bars show SEM.

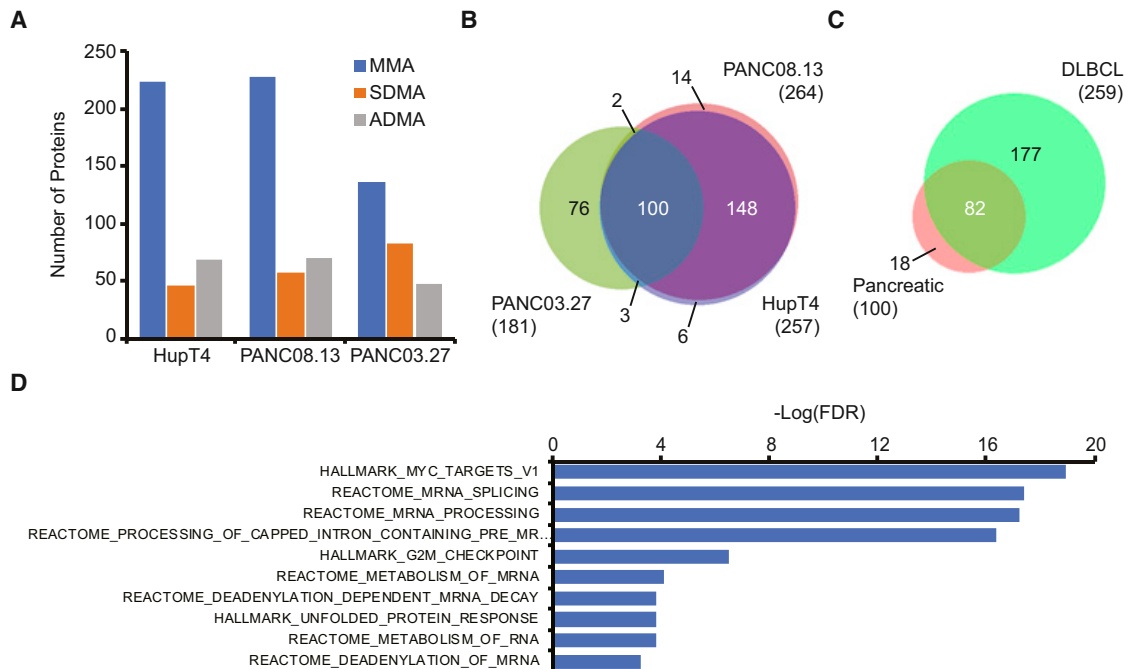


Figure 3. Changes to Arginine Methylation by Type I PRMT Inhibition

(A) Number of proteins with changes to MMA, SDMA, and ADMA by immunoaffinity-enrichment mass spectrometry in pancreatic cancer cell lines after treatment with type I PRMTi.

(B and C) Overlap of proteins with a change in any arginine methyl mark induced by type I PRMTi among pancreatic cell lines (B) or between DLBCL and pancreatic cancer cell lines (C).

(D) MSigDB pathway enrichment for the 82 commonly altered proteins from (C).

See also [Figure S3](#) and [Table S5](#).

range of solid and hematological malignancies and can completely inhibit tumor growth or cause regressions of tumor models *in vivo*.

Identification of Type I PRMT Substrates

To characterize the biological mechanism of action and examine the effect of type I PRMT inhibition on arginine methylation, affinity enrichment proteomics was used to identify proteins with altered ADMA, SDMA, or MMA (Stokes et al., 2012). Following enrichment using antibodies specific for each methylation state from cell lines treated with type I PRMT inhibitor, purified peptides were identified by mass spectrometry and fold changes in enrichment were calculated relative to DMSO-treated cells (see the [STAR Methods](#) for details). Among the DLBCL and pancreatic cancer cell lines analyzed, type I PRMT inhibition altered arginine methylation marks on 445 unique proteins (Figures 3A and S3A; Table S5). Mass spectrometry of KHDRBS1 (Cote et al., 2003), a previously described PRMT1 substrate and also identified in our datasets, confirmed that type I PRMTi inhibits ADMA at arginine 291 (Figures S3B and S3C).

Of 349 total proteins with any change in arginine methylation identified among the pancreatic cell lines, 100 were found in all three (Figure 3B). Similarly, of 276 total proteins identified in the Toledo and OCI-Ly1 DLBCL cell lines, 259 were common between the two (Figure S3D). Moreover, 82 proteins were shared across both histologies, suggesting that type I PRMTs regulate a core set of biological processes (Figure 3C; Table S5). Pathway analysis of these proteins showed enrichment in mRNA processing and splicing, several components of the mRNA cap binding complex (including EIF4G1 and EIF4H), as well as a ribosomal subunit and known target of PRMT5, RPS10 (Ren et al., 2010) (Figure 3D). In addition to mRNA processing and splicing proteins, type I PRMTi altered the arginine methylation of MYC targets. Notably, the MYC pathway also includes numerous splicing and RNA binding proteins, suggesting effects on splicing machinery through multiple mechanisms.

Type I PRMT Inhibition Alters Splicing

The common proteins with arginine methylation changes identified by affinity enrichment proteomics spanned multiple steps of pre-mRNA processing, and include known regulators of exon

(E and F) *In vitro* dose-response curve (E) and average tumor volumes of mice treated once daily with type I PRMTi (GSK3368715) (F) for the BxPC3 cell line. In (F), $n = 10$ animals per group and error bars show SEM.

(G) Individual tumor growth curves of a PDX model of pancreatic adenocarcinoma with once-daily administration of 150 or 300 mg/kg type I PRMTi (GSK3368712; $n = 9-10$ per group).

See also [Figure S2](#) and [Tables S3](#) and [S4](#).

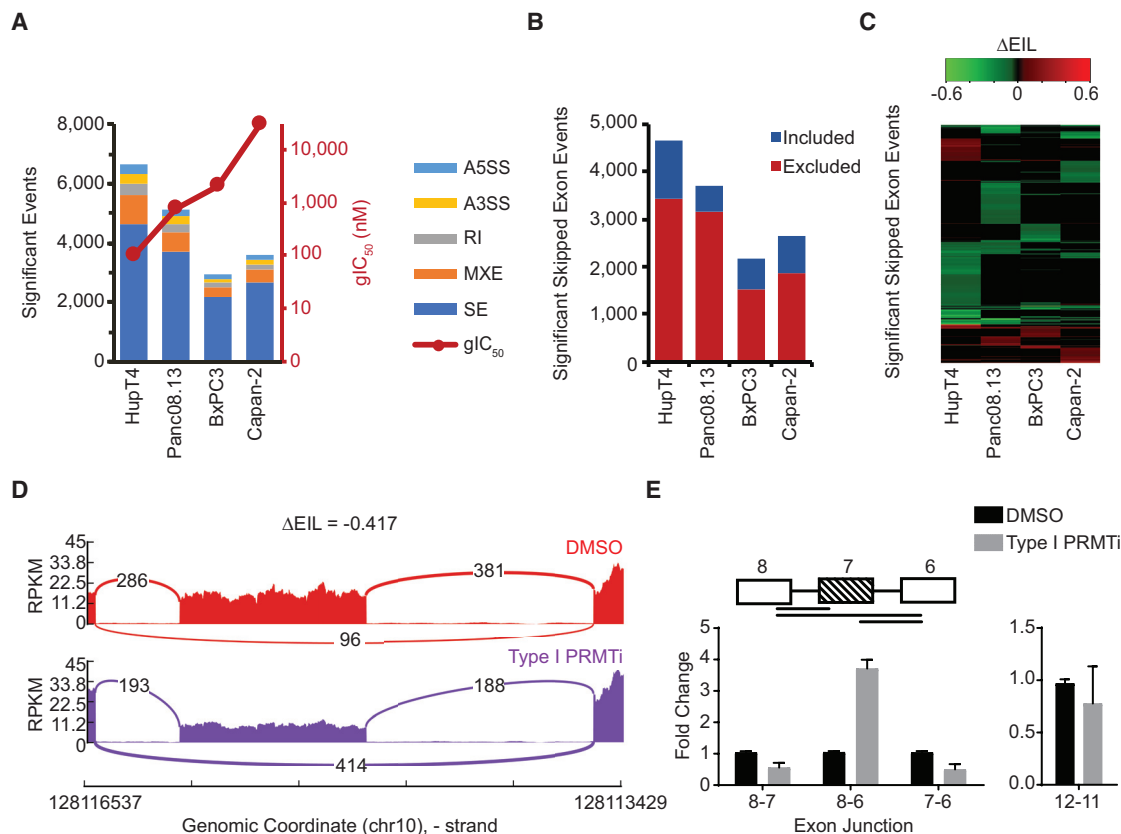


Figure 4. Changes to Splicing by Type I PRMT Inhibition

(A) Total splicing alterations in pancreatic cancer cell lines, plotted against type I PRMT (GSK3368715) gIC₅₀. A5SS, alternative 5' splice site; A3SS, alternative 3' splice site; RI, retained intron; MXE, mutually exclusive exons; SE, skipped exon.

(B) Directionality of exon skipping in pancreatic cell lines, where negative (red) and positive (blue) ΔEIL values represent exon exclusion or inclusion, respectively.

(C) Heatmap of ΔEIL values of exon-skipping events from pancreatic cell lines.

(D) Sashimi plot illustrating multivariate analysis of transcript splicing output for exons 6–8 of *MKI67* from DMSO and type I PRMTi-treated Panc08.13 cell line from a representative replicate of RNA-seq (ΔEIL = -0.417). Numbers over the lines connecting exons represent the number of reads mapping to that junction.

(E) qRT-PCR validation of *MKI67* exon 7 skipping, normalized to exons 11–12, where differential splicing was not detected (n = 3; mean ± SEM).

See also Figure S4.

utilization: SFPQ, FUS, and 14 proteins belonging to the heterogeneous nuclear ribonuclear (hnRNP) family (Papasaiakos et al., 2015; Wang et al., 2013). Arginine methylation of hnRNP proteins can regulate interactions with other factors as well as subcellular localization; therefore changes in arginine methylation by type I PRMT inhibition may lead to aberrant exon usage (Gurunathan et al., 2015; Wall and Lewis, 2017). To understand the functional consequences of the switch from ADMA to SDMA or MMA across RNA processing factors, RNA sequencing (RNA-seq) was used to investigate the effects of type I PRMT inhibition on global splicing patterns. Multivariate analysis of transcript splicing (Shen et al., 2014) was used to quantify differential splicing events from RNA-seq of poly(A) selected RNA from a panel of pancreatic cancer cell lines treated with type I PRMTi. Significant splicing alterations were identified in all lines examined, with the cell lines most sensitive to growth inhibition by GSK3368715 showing the greatest number of events (Figure 4A). Skipped exons are the most frequent type of alteration observed in all four cell lines tested, with a bias toward exon exclusion upon inhibitor treatment (Figures 4B and 4C). Select exon-skip-

ping events were validated by RT-qPCR (Figures 4D, 4E, and S4A–S4M). The majority of these events were unique to each cell line, with only 194 common to all lines (Figure 4C). However, compound treatment induced changes in the splicing of genes in common pathways among the lines, including cell cycle and mitosis (Figure S4N). These data suggest that type I PRMT inhibition results in profound changes in cellular splicing, predominantly affecting exon usage.

Anti-proliferative Effects of Combined Type I PRMT and PRMT5 Inhibition

PRMT5 is the type II PRMT that catalyzes the bulk of cellular SDMA and is known to share substrates with PRMT1 (Zheng et al., 2013). PRMT5 is overexpressed in a number of tumor types, and selective PRMT5 inhibitors have recently entered clinical trials. To determine the effects of combined inhibition of type I PRMTs and PRMT5 on cancer cell proliferation, a panel of cell lines was treated with GSK3368715 and the PRMT5 inhibitor GSK3203591 (Gerhart et al., 2018) across a range of concentrations. In the pancreatic cancer cell lines tested, increasing fixed

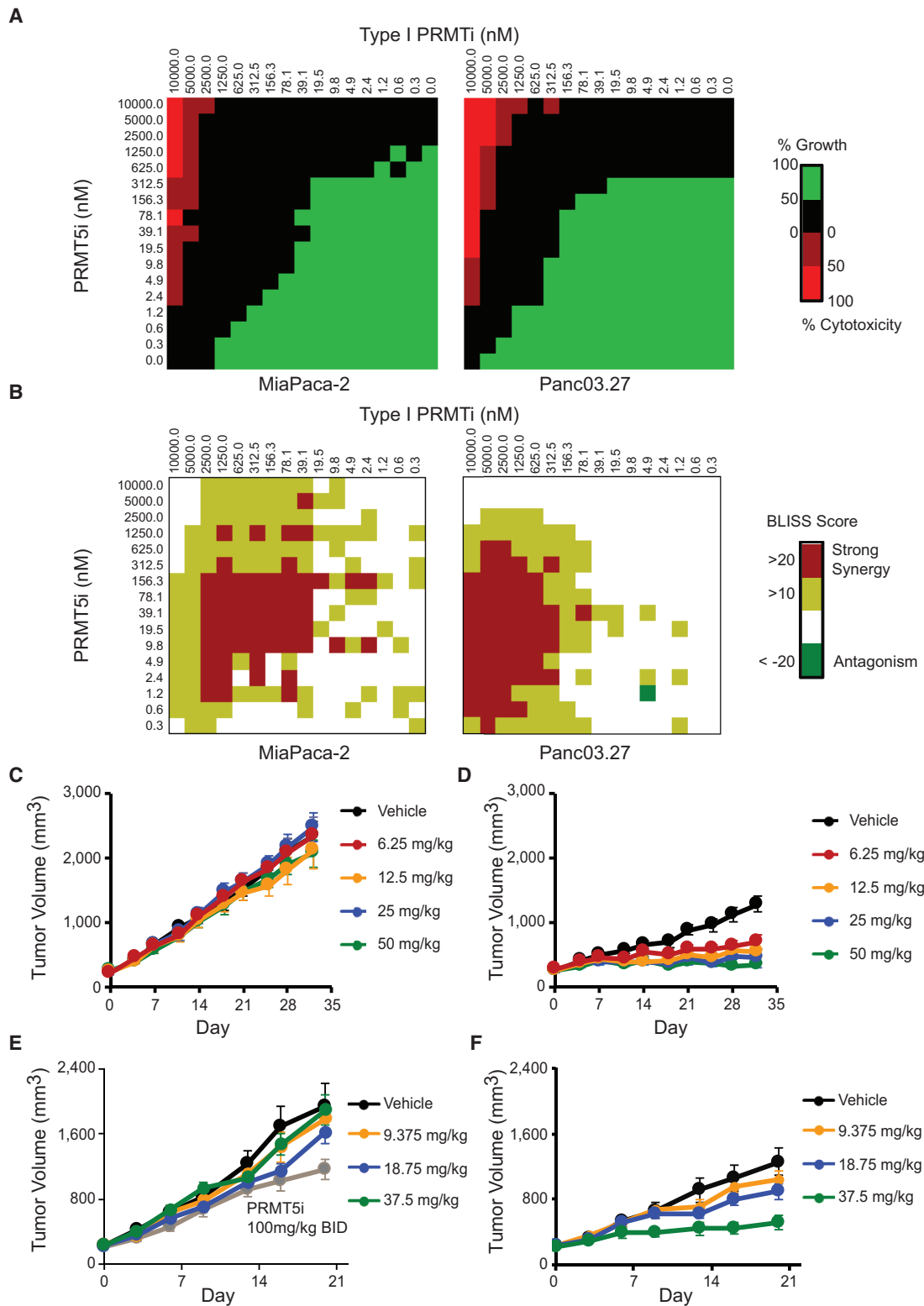


Figure 5. Combined Anti-proliferative Effects of Type I PRMT and PRMT5 Inhibition

(A and B) Average growth death index (A) and Bliss score (B) for type I PRMTi (GSK3368715) and PRMT5i (GSK3203591) double titrations ($n \geq 2$ per cell line). (C and D) Average tumor volumes of MiaPaca-2 xenografts after once-daily administration of PRMT5i (GSK3326595) alone (C) or in combination with once-daily administration of 150 mg/kg type I PRMTi (GSK3368715) (D). For each group, $n = 10$; mean \pm SEM.

(legend continued on next page)

concentrations of each inhibitor enhanced the potency of the other (Figures S5A and S5B). Furthermore, combination treatment produced cytotoxic responses at concentrations at which either single agent was cytostatic (Figures 5A, S5C, and S5D). To determine if the effects on cell growth are synergistic, the Bliss model was used to calculate synergy scores using the effects from single-agent treatment to estimate the outcome of an additive effect (Fouquier and Guedj, 2015). Bliss scores of >10 were classified as synergistic and >20 as strongly synergistic. The combination of type I PRMTi and GSK3203591 elicited strong synergistic effects on net cell growth in pancreatic cancer and DLBCL cell lines across a range of concentrations (Figures 5B, S5C, and S5D). The addition of 10 or 100 nM GSK3203591, which had no effect on growth as monotherapy, increased the potency of type I PRMT inhibition coincident with enhanced caspase-3/7 cleavage, reflecting activation of apoptotic cell death (Figure S5E).

To evaluate the efficacy and tolerability of this combination *in vivo*, mice bearing MiaPaca-2 pancreatic adenocarcinoma xenografts were dosed with type I PRMTi (GSK3368715) or the PRMT5 inhibitor, GSK3326595, either alone or titrated in combination with a fixed concentration of the other. As monotherapies, the highest doses of type I PRMTi and PRMT5i produced significant, but incomplete, effects on tumor growth. Once-daily dosing of 200 mg/kg of PRMT5 inhibitor yielded comparable results to twice-daily 100 mg/kg dosing. Lower doses of each did not significantly affect tumor growth (Figures 5C–5F, S5F, and S5G; Table S6). In both experiments, combinations significantly enhanced the inhibition of tumor growth relative to either single agent alone at all doses tested. Body-weight of animals dosed with the combination was no different than single-agent treatment in either study, suggesting the combination was well tolerated (Figures S5H and S5I; Table S6).

Effects of Combined PRMT Inhibition on Arginine Methylation and Global Splicing

Previous studies have shown that inhibition of PRMT5 can alter SDMA on splicing regulators and has profound effects on cellular splicing (Gerhart et al., 2018). To understand the mechanistic basis for the synergy between type I PRMT and PRMT5 inhibition, the effects on arginine methylation of GSK3368715 were assessed in the presence of increasing concentrations of PRMT5i (GSK3203591). While SDMA levels in combination-treated cells were attenuated, they remained below those of DMSO controls (Figure 6A). Accumulation of MMA by the combination was inhibited relative to cells treated with type I PRMTi alone at all concentrations of PRMT5i tested (Figure 6A). In contrast, basal ADMA and MMA states were not affected by PRMT5 inhibition alone. These data suggest that the majority of MMA and SDMA generated upon inhibition of type I PRMT activity depends on the enzymatic activity PRMT5. Consistent with the global changes to arginine methylation observed in western blots, mass spectrometry analysis of KHRDBS1 showed inhibition of

ADMA and SDMA on R291 after treatment with type I PRMT and PRMT5 inhibitors either individually or in combination (Figures 6B and S6). Combined inhibition of type I PRMTs and PRMT5 on individual protein substrates was further explored using mass spectrometry following immunoprecipitation of tryptic peptides with methyl-arginine-specific antibodies. Among peptides that were enriched by MMA or SDMA immunoprecipitation by type I PRMTi alone, 34% and 76% showed a 4-fold lower induction of MMA or SDMA, respectively, upon addition of PRMT5i (Figures 6C and 6D; Table S7). These data suggest that combined inhibition of type I PRMTs and PRMT5 produces a reduced state of arginine methylation and may manifest in differential effects on the function of type I PRMT substrates relative to inhibition by either inhibitor alone.

To understand the functional consequences of the global methylation state induced by the combination of inhibitors, RNA-seq was used to compare splicing alterations in the Panc03.27 cell line between single-agent and combination treatment. Both single agents had significant effects on all categories of splicing, with exon skipping being the most frequent (Figures 6E and 6F). The total numbers of skipped exons were similar between type I PRMTi (1,405) and PRMT5i (1,400), and 260 were induced by both compounds (Figure 6G). The combination induced 3,730 exon-skipping events, with 822 (22%) and 724 (19%) shared with type I PRMTi and PRMT5i, respectively, and 219 (6%) common to all three conditions (Figure 6G). These data suggest that the inhibition of PRMT5 exacerbates the effect of type I PRMT inhibition on alternative splicing by attenuating the accumulation of MMA and SDMA.

MTAP Deficiency Is a Predictive Marker of Sensitivity to Type I PRMT Inhibition

Recent studies have described a mechanism by which loss of *MTAP* leads to increased levels of its metabolite MTA, which has previously been characterized as a selective and potent inhibitor of PRMT5 activity, resulting in lower cellular levels of SDMA (Kryukov et al., 2016; Marjon et al., 2016; Mavrakis et al., 2016). Given the synergistic effects of type I PRMTi and exogenous PRMT5 inhibitors on the proliferation of cancer cell lines, *MTAP* deletion may offer a scenario to achieve a cancer cell-intrinsic combination of GSK3368715 with PRMT5 inhibition. Of 212 cell lines in which *MTAP* status was determined by DNA copy-number variation and mRNA or protein expression levels, 56 were deficient in *MTAP* (Table S8). The association between *MTAP* deficiency and sensitivity to GSK3368715 was apparent in select tumor types. Median glC_{50} values of GSK3368715 were ≥ 6 -fold lower in *MTAP*-deficient lymphoma, melanoma, and pancreatic cancer cell lines relative to wild-type (WT) cell lines. Interestingly, among this panel of pancreatic cell lines, only *MTAP*-deficient lines exhibited a cytotoxic response to type I PRMTi (Figures 7A and 7B; Table S8). Addition of exogenous MTA increased the potency of type I PRMTi 10-fold in 9/19 pancreatic cancer cell lines, an effect that was exaggerated

(E and F) Tumor volumes of MiaPaca-2 xenografts after once-daily administration of type I PRMTi alone (E) or in combination with once-daily administration of 200 mg/kg PRMT5i (F). For comparison, 100 mg/kg twice-daily dose of PRMT5i is shown in (E) as gray dotted line. For each group, $n = 10$; mean \pm SEM.

See also Figure S5 and Table S6.

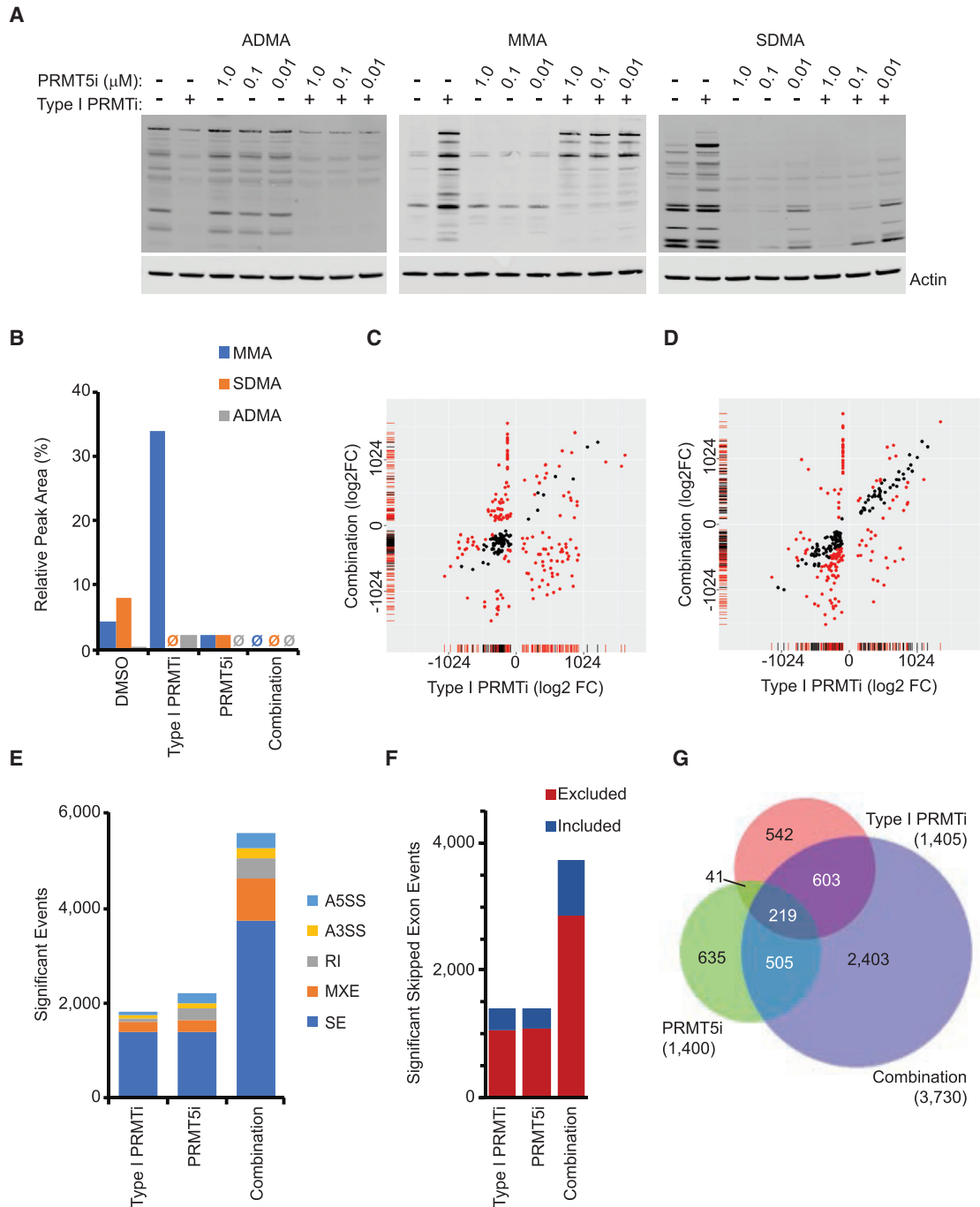


Figure 6. Combined Effects of Type I PRMT and PRMT5 Inhibition on Induction of MMA and SDMA

(A) Effect of type I PRMTi (GSK3368715) and PRMT5i (GSK3203591) combination on global arginine methylation levels in the Panc03.27 cell line. Representative western blot image of two independent experiments. Lanes marked with a “+” and “-” indicate treatment with or without 2 μM type I PRMTi, respectively.

(B) Validation of arginine methylation changes induced by single agents and combination on R291 of immunopurified KHDRBS1 by mass spectrometry in Panc03.27 cell line; average of two independent experiments.

(C and D) Scatterplot comparing fold changes of SDMA (C) and MMA (D) on individual peptides between type I PRMTi alone and in combination with PRMT5i (GSK3203591). Red dots are peptides with ≥ 4-fold differences between two conditions.

(E) Splicing alterations after single-agent and combination treatment in the Panc03.27 parental cell line.

(F) Directionality of exon skipping in Panc03.27 following single-agent or combination treatment.

(G) Overlap of exon-skipping events shown in (F).

See also [Figure S6](#) and [Table S7](#).

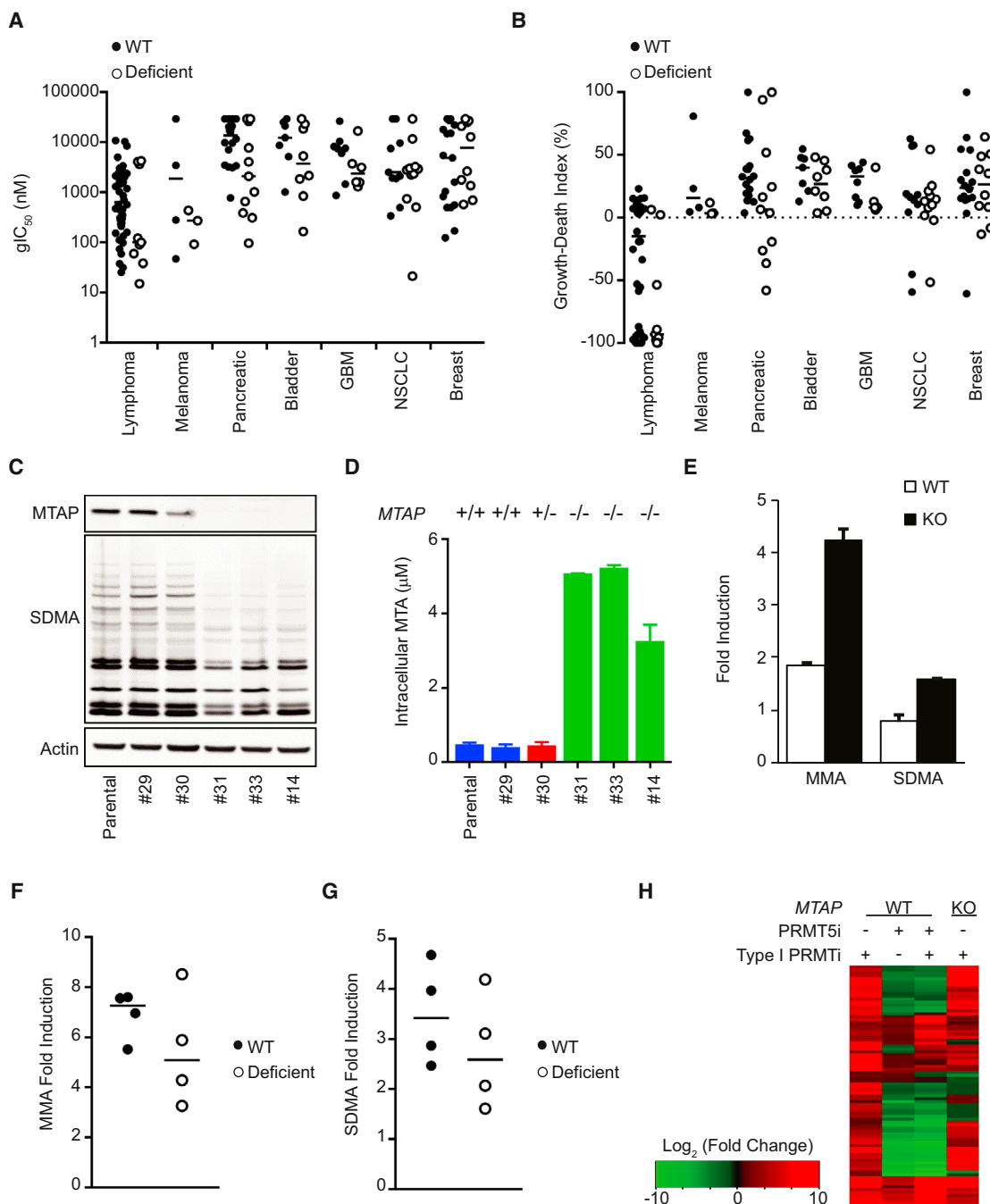


Figure 7. *MTAP* Deficiency Is a Predictive Marker of Sensitivity to Type I PRMT Inhibition

(A and B) Comparison of GSK3368715 gIC₅₀ (A) and growth death index (B) in *MTAP* WT or-deficient cell lines. Black lines represent median values. Dotted line in (B) indicates complete cytostasis.

(C) Representative western blot showing levels of *MTAP* and *SDMA* in Panc03.27 parental and CRISPR clones targeting the *MTAP* locus.

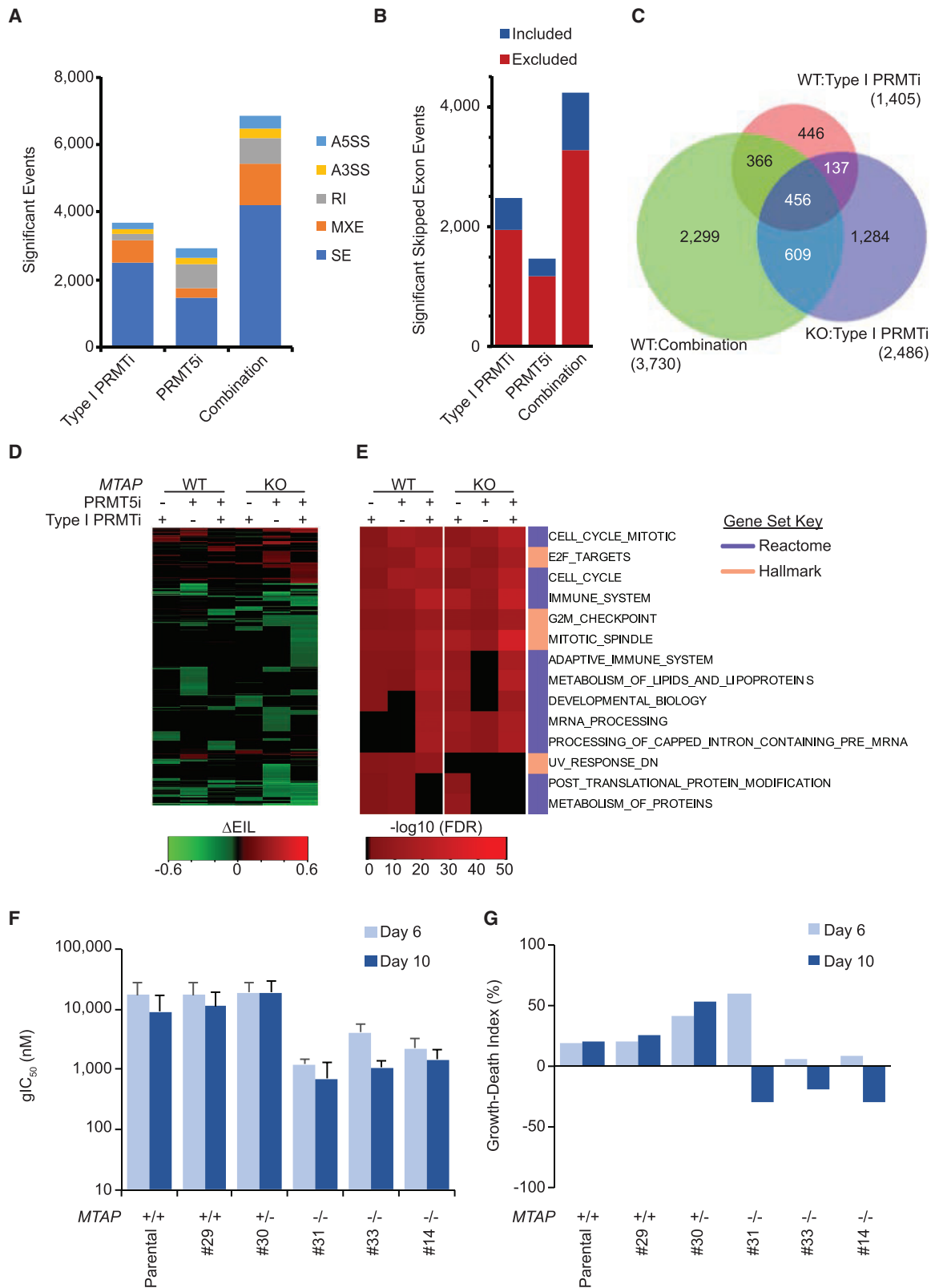
(D) Intracellular MTA levels ($n = 3$ measurements per cell line) in each line from (C); mean \pm SEM.

(E) Maximum fold induction of MMA and *SDMA* by type I PRMTi in isogenic Panc03.27 *MTAP* wild-type (WT) and deficient (KO) cell lines ($n = 2$ in each cell line; mean \pm SEM).

(F and G) Average fold induction of MMA (F) and *SDMA* (G) by type I PRMTi (GSK3368712) in a panel of *MTAP* WT and deficient pancreatic cell lines ($n = 2$ experiments in each cell line). Black lines represent medians of data.

(H) Heatmap of *SDMA* induction on individual peptides in parental Panc03.27 cells (WT) with single agents and combination treatment and Panc03.27 *MTAP*^{KO/KO} cell line (KO) with type I PRMTi alone.

See also Figure S7 and Tables S7 and S8.



(legend on next page)

among the cell lines with *MTAP* deficiency (Figure S7A). In a panel of lymphoma, pancreatic, and breast cancer cell lines, *MTAP* deficiency was associated with increased intracellular MTA and decreased SDMA levels relative to WT cell lines (Figures S7B and S7C). *MTAP*-deficient breast cancer cell lines had decreased SDMA and comparable intracellular MTA concentrations to deficient lymphoma and pancreatic cell lines, despite there being no association with sensitivity to GSK3368715 by *MTAP* status in this tumor type.

To specifically evaluate the relationship between *MTAP* and type I PRMT inhibition, CRISPR-mediated deletion was utilized to generate *MTAP*-deficient lines from an *MTAP* WT pancreatic cell line that showed minimal and cytostatic anti-proliferative response to type I PRMTi, Panc03.27 (glC₅₀, 12 μM). Lack of *MTAP* protein, increased intracellular MTA levels, and decreased SDMA relative to the control line was confirmed in three independent clones (Figures 7C and 7D). Despite comparable reduction of ADMA in an *MTAP* isogenic clone by type I PRMTi, the induction of MMA was attenuated in an *MTAP*-deficient clone (no. 31, hereafter referred to as *MTAP*^{KO/KO}); SDMA showed no induction and remained at the level of controls (Figures 7E and S7D). Similarly, the median fold induction of both MMA and SDMA by type I PRMT inhibition was lower among pancreatic cell lines with *MTAP* deficiency compared with WT cell lines (Figures 7F, 7G, S7E, and S7F). Addition of PRMT5 inhibitor (GSK3203591) led to comparable, nearly complete reduction of SDMA in both the parental Panc03.27 cell line and the *MTAP*^{KO/KO} clone (Figure S7G), indicating that PRMT5 activity is only partially inhibited at the concentrations of MTA present in *MTAP*-deficient cell lines. Consistent with this hypothesis, proteome scale profiling of immunoprecipitated SDMA-containing peptides from the *MTAP*^{KO/KO} clone by mass spectrometry revealed a partial attenuation of SDMA induction by type I PRMTi of the subset of peptides that increased SDMA in the WT cell line (Figure 7H; Table S7). In contrast, *MTAP* WT cells treated with the combination of type I PRMTi and PRMT5i showed a similar effect to PRMT5 inhibition alone.

To understand the functional consequence of partial PRMT5 inhibition through *MTAP* deletion, splicing was characterized in the Panc03.27 *MTAP*^{KO/KO} clone. Type I PRMTi induced 2,486 exon-skipping events in the *MTAP*^{KO/KO} cell line, in contrast to 1,405 in the parental cell line (Figures 8A, 8B, and 6F). Among the skipped exon events in the *MTAP* isogenic clone, 593 (24%) and 1,065 (43%) overlapped with those observed in WT cell line treated with type PRMTi or the combination, respectively (Figures 8C and 8D). In both cell lines, single-agent treatments affected the splicing of genes involved in cell cycle and mitosis pathways (Figure 8E). Type I PRMTi elicited splicing alterations

of genes involved in mRNA processing and splicing pathways, overlapping with those the combination achieved in both cell lines. Therefore, splicing of genes within this pathway may be most susceptible to inhibition of both arginine methylation pathways. These data suggest that type I PRMT inhibition can yield comparable effects on splicing when combined with PRMT5 inhibition through either an exogenous, small-molecule inhibitor of PRMT5, or the accumulation of MTA in *MTAP*-deficient cell lines.

To specifically determine whether *MTAP* deletion would sensitize Panc03.27 cells to type I PRMT inhibition, the effect of GSK3368712 on the growth of *MTAP* isogenic clones was evaluated. *MTAP* deficiency resulted in 7- and 12-fold decrease in glC₅₀ of type I PRMTi after 6 and 10 days of culture, respectively (Figure 8F). Furthermore, type I PRMTi induced cytotoxic responses after 10 days of culture, whereas the parental cell line and control clones remained cytostatic (Figure 8G). Notably, heterozygous mutation of *MTAP* had no effect on SDMA, intracellular MTA levels, or sensitivity to type I PRMTi, despite a reduction in *MTAP* protein levels. Collectively, these data suggest that partial inhibition of PRMT5 activity through *MTAP* deficiency can reveal enhanced sensitivity of cancer cells to type I PRMT inhibition.

DISCUSSION

The clinical success of targeted therapies can be increased by identifying patient populations most likely to benefit from these potential medicines. Biomarker-driven approaches not only increase the likelihood of clinical trial success but also offer a paradigm for personalized medicine in providing effective therapeutic interventions for patients based on the characteristics of their disease. In this report, we present a strategy for maximizing the anti-tumor activity of an agent through a mechanism-based biomarker approach. GSK3368715 is a potent, reversible, SAM uncompetitive inhibitor of type I PRMTs that produces a shift in arginine methylation states on hundreds of substrates from ADMA to MMA and SDMA. As a monotherapy, GSK3368715 induces anti-proliferative effects on cell lines from a broad range of hematological and solid tumor types *in vitro* and inhibits growth of tumor models *in vivo*.

Combination with a PRMT5 inhibitor attenuates the accumulation of MMA and SDMA induced by type I PRMT inhibition, and results in profound effects on alternative splicing distinct from those observed with either single agent. These observations suggest that, whereas ADMA, MMA, or SDMA may modulate specific activities of splicing regulatory factors including hnRNP family proteins, the lack of arginine methylation induced by the combination may have more drastic consequences on protein

Figure 8. Effect of *MTAP* Deficiency on Splicing

(A and B) All splicing alterations (A) and directional changes in exon skipping (B) in *MTAP*-deficient Panc03.27 cell line with single agents or combination. (C) Overlap between changes induced by type I PRMTi (GSK3368712) alone in the *MTAP*-deficient Panc03.27 line (KO) compared with single-agent and combination treatment in the Panc03.27 parental cell line (WT); numbers in parentheses are the total number of significant exon-skipping events in that cell line and condition. (D) Heatmap comparing all exon-skipping events shown in (C). (E) Pathway enrichments for significant exon-skipping events for both cell lines after single-agent and combination treatment. In (D) and (E), columns marked with a + represent samples treated with PRMT5i (0.5 μM) or type I PRMTi (2 μM) as indicated, whereas “-” are samples that do not have the respective inhibitor added. (F and G) Six- and 10-day type I PRMTi glC₅₀ (F) and growth death index (G) for Panc03.27 control (WT) and *MTAP*-deficient clones (KO; n = 3 experiments per cell line; mean ± SEM).

function than a switch in methylation states upon inhibition of type I PRMT activity alone. Consistent with this hypothesis, the number of exon-skipping events dramatically increased with combination treatment relative to either single agent, suggesting a more profound effect on regulators of exon usage. Moreover, the global state of low arginine methylation produced by combination treatment is associated with synergistic effects on the proliferation and viability of cancer cell lines, further suggesting that attenuating the compensatory induction of MMA and SDMA through PRMT5 inhibition further sensitizes cancer cells to type I PRMT inhibition by GSK3368715. Reports have suggested that splicing may be a vulnerability in splicing mutant myelodysplastic syndrome and acute myeloid leukemias, as well as MYC-driven cancers (Dvinge et al., 2016; Hsu et al., 2015, 2017), therefore, further compromising splicing through combining type I PRMT and PRMT5 inhibition may provide a compelling approach to exploit a sensitivity common to a range of human tumor types. Given that both classes of PRMT inhibitors are in currently in clinical development (NCT03573310, NCT02783300, and NCT03614728), this combination opportunity offers a relevant and timely therapeutic strategy for cancer patients.

The mechanism underlying the anti-tumor activity of the type I PRMT and PRMT5 inhibitor combination provides a rationale to explore *MTAP* deficiency as predictive of sensitivity to GSK3368715. Although *MTAP* deficiency has been hypothesized as a vulnerability to PRMT5 depletion, small-molecule inhibition of PRMT5 has not recapitulated this effect, potentially due to the opposing inhibitory mechanisms of MTA (SAM competitive) and the current small-molecule inhibitors (SAM uncompetitive) (Marjon et al., 2016). Importantly, diminished SDMA among *TAP*-deficient lines suggests that sufficient concentration of MTA is achieved to at least partially inhibit PRMT5 activity. As predicted by the synergistic anti-tumor activity through combined inhibition of type I PRMTs with PRMT5, *MTAP* deficiency is associated with decreased induction of MMA and SDMA upon inhibition of type I PRMT activity, and this correlates with sensitivity of cell lines to growth inhibition to GSK3368715. Furthermore, in pancreatic cancer cell lines, *MTAP* deletion is associated with cytotoxic responses to GSK3368715, an effect that can be recapitulated by disruption of the *MTAP* locus in a WT cell line. These data demonstrate that the anti-tumor activity of GSK3368715 is enhanced through PRMT5 inhibition and suggest that this combination may be achieved through tumor-specific accumulation of MTA. *MTAP* is located near the tumor suppressor gene *CDKN2A*, and thus is frequently deleted in human cancers, including 40% of glioblastoma, 25% of melanoma and pancreatic adenocarcinoma, and 15% of non-small-cell lung carcinoma (Kryukov et al., 2016; Marjon et al., 2016; Mavrakis et al., 2016). Given that this substantial population includes many tumor types with limited therapeutic options, inhibition of type I PRMT activity by GSK3368715 may represent a promising approach for tumors of high unmet medical need with a defined patient selection strategy. Despite comparable intracellular MTA concentrations in *MTAP*-deficient cell lines across multiple histologies, the correlation with *MTAP* loss and sensitivity to GSK3368715 varies by tumor type. Therefore, additional factors could contribute to the sensitivity of *MTAP*-deficient cancers and will require clinical investigation to further

elucidate. The safety, tolerability, and PK profile of GSK3368715 is currently under clinical investigation and the potential therapeutic benefit for cancer patients will soon be determined (NCT03666988).

STAR★METHODS

Detailed methods are provided in the online version of this paper and include the following:

- KEY RESOURCES TABLE
- CONTACT FOR REAGENT AND RESOURCE SHARING
- EXPERIMENTAL MODELS AND SUBJECT DETAILS
 - Tumor Growth Assessment of Human Tumor Xenografts
 - Toxicology Assessment
 - DLBCL Colony Formation Assays
 - Cell Lines
 - Generation of *MTAP*-Deficient Clones
- METHOD DETAILS
 - Synthesis of GSK3368715
 - Synthesis of GSK3368712
 - High Throughput Screen
 - PRMT Biochemical Assays
 - Methyltransferase Biochemical Assays
- QUANTIFICATION AND STATISTICAL ANALYSIS
- DATA AND SOFTWARE AVAILABILITY

SUPPLEMENTAL INFORMATION

Supplemental Information can be found online at <https://doi.org/10.1016/j.ccell.2019.05.014>.

ACKNOWLEDGMENTS

The authors would like to thank Natalie Karpinch for proof reading of the final manuscript.

AUTHOR CONTRIBUTIONS

GlaxoSmithKline: A.F. designed, performed, and oversaw experiments, analyzed data, and wrote the manuscript. S.R.R. performed bioinformatic analysis of splicing and proteomic data. S.O., S.V.G., N.S., J.L., and R.N. performed cellular experiments. M.B.P. designed, performed, and analyzed biochemistry experiments. Y.L., M.B., and S.K. performed *in vivo* experiments. C.F.McH. oversaw *in vivo* experiments and performed and analyzed PK experiments. C.W. performed mass spectrometry of KHRDBS1. C.W., F.Z., and R.A. analyzed mass spectrometry data. N.O.O. analyzed X-ray crystallography results. N.D.A. designed, performed, and analyzed data from chemistry experiments. R.A.T. and T.K.H. designed and interpreted safety studies. C.L.C., C.C., M.T.McC., R.K.P., R.G.K., and O.B. contributed to design of studies and interpretation of data. H.P.M. designed and oversaw experiments, interpreted data, and wrote manuscript.

Epizyme: N.R. and N.W. designed PK experiments, oversaw bioanalytical data, and interpreted data. T.L. performed cellular experiments and interpreted data. C.A. and D.J. performed cellular experiments. A.R. designed and oversaw cellular experiments and interpreted data. S.A.R. and J.J.S. designed and oversaw cellular and *in vivo* pharmacology experiments and interpreted data. M.P.S. and S.J.-O'H. designed and performed biochemical experiments and interpreted data. T.R. designed and performed biochemical experiments. K.S. designed and oversaw X-ray crystallography experiments. A.B.-S. designed protein constructs, designed and oversaw X-ray crystallography experiments. K.S. designed *in vivo* pharmacology experiments and interpreted data. J.M. performed molecular modeling and cheminformatics

that led to design of lead inhibitors. J.C. designed molecules and oversaw chemistry synthesis. L.H.M., R.C., and G.S. designed molecules, oversaw chemistry synthesis, and interpreted data. R.A.C. and M.P.M. interpreted data. All authors reviewed the manuscript.

DECLARATION OF INTERESTS

A.F., S.R.R., S.O., S.V.G., N.D.A., M.B.P., N.S., J.L., Y.L., M.B., S.K., C.F.M., M.T.McC., R.N., C.W., F.Z., R.A., N.O.O., R.A.T., T.K.H., C.L.C., C.C., R.K.P., R.G.K., O.B., and H.P.M. were or are employees of GlaxoSmithKline. L.H.M., N.R., T.L., S.A.R., J.J.S., R.A.C., M.P.M., J.C., K.S., J.M., S.J.-O., C.A., D.J., A.R., M.P.S., N.W., K.S., A.B.-S., T.R., G.S., and R.C. were or are employees of Epizyme. A.F., S.O., S.V.G., N.S., J.L., R.G.K., O.B., and H.P.M. are listed as inventors on one or several of the following patents related to this work: IB2017/057546, IB2017/057550.

Received: February 4, 2019

Revised: April 5, 2019

Accepted: May 24, 2019

Published: June 27, 2019

REFERENCES

- Almeida-Rios, D., Graca, I., Vieira, F.Q., Ramalho-Carvalho, J., Pereira-Silva, E., Martins, A.T., Oliveira, J., Goncalves, C.S., Costa, B.M., Henrique, R., and Jeronimo, C. (2016). Histone methyltransferase PRMT6 plays an oncogenic role of in prostate cancer. *Oncotarget* 7, 53018–53028.
- Altan, B., Yokobori, T., Ide, M., Mochiki, E., Toyomasu, Y., Kogure, N., Kimura, A., Hara, K., Bai, T., Bao, P., et al. (2015). Nuclear PRMT1 expression is associated with poor prognosis and chemosensitivity in gastric cancer patients. *Gastric Cancer* 19, 789–797.
- Andrews, S. (2010). FastQC: a quality control tool for high throughput sequence data, Available online at: <http://www.bioinformatics.babraham.ac.uk/projects/fastqc>
- Bedford, M.T., and Clarke, S.G. (2009). Protein arginine methylation in mammals: who, what, and why. *Mol. Cell* 33, 1–13.
- Brostoff, S., and Eylar, E.H. (1971). Localization of methylated arginine in the A1 protein from myelin. *Proc. Natl. Acad. Sci. U S A* 68, 765–769.
- Chan-Penebre, E., Kuplast, K.G., Majer, C.R., Boriack-Sjodin, P.A., Wigle, T.J., Johnston, L.D., Rioux, N., Munchhof, M.J., Jin, L., Jacques, S.L., et al. (2015). A selective inhibitor of PRMT5 with in vivo and in vitro potency in MCL models. *Nat. Chem. Biol.* 11, 432–437.
- Cheung, N., Chan, L.C., Thompson, A., Cleary, M.L., and So, C.W. (2007). Protein arginine-methyltransferase-dependent oncogenesis. *Nat. Cell Biol.* 9, 1208–1215.
- Cote, J., Boisvert, F.M., Boulanger, M.C., Bedford, M.T., and Richard, S. (2003). Sam68 RNA binding protein is an in vivo substrate for protein arginine N-methyltransferase 1. *Mol. Biol. Cell* 14, 274–287.
- Dhar, S., Vemulapalli, V., Patananan, A.N., Huang, G.L., Di Lorenzo, A., Richard, S., Comb, M.J., Guo, A., Clarke, S.G., and Bedford, M.T. (2013). Loss of the major type I arginine methyltransferase PRMT1 causes substrate scavenging by other PRMTs. *Sci. Rep.* 3, 1311.
- Dobin, A., Davis, C.A., Schlesinger, F., Drenkow, J., Zaleski, C., Jha, S., Batut, P., Chaisson, M., and Gingeras, T.R. (2013). STAR: ultrafast universal RNA-seq aligner. *Bioinformatics* 29, 15–21.
- Dvinge, H., Kim, E., Abdel-Wahab, O., and Bradley, R.K. (2016). RNA splicing factors as oncoproteins and tumour suppressors. *Nat. Rev. Cancer* 16, 413–430.
- Elakoum, R., Gauchotte, G., Oussalah, A., Wissler, M.P., Clement-Duchene, C., Vignaud, J.M., Gueant, J.L., and Namour, F. (2014). CARM1 and PRMT1 are dysregulated in lung cancer without hierarchical features. *Biochimie* 97, 210–218.
- Eng, J.K., McCormack, A.L., and Yates, J.R. (1994). An approach to correlate tandem mass spectral data of peptides with amino acid sequences in a protein database. *J. Am. Soc. Mass Spectrom.* 5, 976–989.
- Fouquier, J., and Guedj, M. (2015). Analysis of drug combinations: current methodological landscape. *Pharmacol. Res. Perspect.* 3, e00149.
- Gerhart, S.V., Kellner, W.A., Thompson, C., Pappalardi, M.B., Zhang, X.P., Montes de Oca, R., Penebre, E., Duncan, K., Boriack-Sjodin, A., Le, B., et al. (2018). Activation of the p53-MDM4 regulatory axis defines the anti-tumour response to PRMT5 inhibition through its role in regulating cellular splicing. *Sci. Rep.* 8, 9711.
- Greenblatt, S.M., Liu, F., and Nimer, S.D. (2016). Arginine methyltransferases in normal and malignant hematopoiesis. *Exp. Hematol.* 44, 435–441.
- Greenblatt, S.M., Man, N., Hamard, P.J., Asai, T., Karl, D., Martinez, C., Bilbao, D., Stathais, V., McGrew-Jermacowicz, A., Duffort, S., et al. (2018). CARM1 is essential for myeloid leukemogenesis but dispensable for normal hematopoiesis. *Cancer Cell* 33, 1111–1127.e5.
- Guo, A., Gu, H., Zhou, J., Mulhern, D., Wang, Y., Lee, K.A., Yang, V., Aguiar, M., Kornhauser, J., Jia, X., et al. (2014). Immunoaffinity enrichment and mass spectrometry analysis of protein methylation. *Mol. Cell. Proteomics* 13, 372–387.
- Gurunathan, G., Yu, Z., Coulombe, Y., Masson, J.Y., and Richard, S. (2015). Arginine methylation of hnRNPUL1 regulates interaction with NBS1 and recruitment to sites of DNA damage. *Sci. Rep.* 5, 10475.
- Hsu, J.H., Hubbell-Engler, B., Adelmant, G., Huang, J., Joyce, C.E., Vazquez, F., Weir, B.A., Montgomery, P., Tsherniak, A., Giacomelli, A.O., et al. (2017). PRMT1-mediated translation regulation is a crucial vulnerability of cancer. *Cancer Res.* 77, 4613–4625.
- Hsu, T.Y., Simon, L.M., Neill, N.J., Marcotte, R., Sayad, A., Bland, C.S., Echeverria, G.V., Sun, T., Kurley, S.J., Tyagi, S., et al. (2015). The spliceosome is a therapeutic vulnerability in MYC-driven cancer. *Nature* 525, 384–388.
- Hulsen, T., de Vlieg, J., and Alkema, W. (2008). BioVenn - a web application for the comparison and visualization of biological lists using area-proportional Venn diagrams. *BMC Genomics* 9, 488.
- Kryukov, G.V., Wilson, F.H., Ruth, J.R., Paulk, J., Tsherniak, A., Marlow, S.E., Vazquez, F., Weir, B.A., Fitzgerald, M.E., Tanaka, M., et al. (2016). MTAP deletion confers enhanced dependency on the PRMT5 arginine methyltransferase in cancer cells. *Science* 351, 1214–1218.
- Li, H., Handsaker, B., Wysoker, A., Fennell, T., Ruan, J., Homer, N., Marth, G., Abecasis, G., and Durbin, R.; Genome Project Data Processing Subgroups (2009). The sequence alignment/map format and SAMtools. *Bioinformatics* 25, 2078–2079.
- MacLean, B., Tomazela, D.M., Shulman, N., Chambers, M., Finney, G.L., Frewen, B., Kern, R., Tabb, D.L., Liebner, D.C., and MacCoss, M.J. (2010). Skyline: an open source document editor for creating and analyzing targeted proteomics experiments. *Bioinformatics* 26, 966–968.
- Marjon, K., Cameron, M.J., Quang, P., Clasquin, M.F., Mandley, E., Kunii, K., McVay, M., Choe, S., Kernysky, A., Gross, S., et al. (2016). MTAP deletions in cancer create vulnerability to targeting of the MAT2A/PRMT5/RIOK1 axis. *Cell Rep.* 15, 574–587.
- Mavrikis, K.J., McDonald, E.R., 3rd, Schlabach, M.R., Billy, E., Hoffman, G.R., deWeck, A., Ruddy, D.A., Venkatesan, K., Yu, J., McAllister, G., et al. (2016). Disordered methionine metabolism in MTAP/CDKN2A-deleted cancers leads to dependence on PRMT5. *Science* 351, 1208–1213.
- McCabe, M.T., Ott, H.M., Ganji, G., Korenchuk, S., Thompson, C., Van Aller, G.S., Liu, Y., Graves, A.P., Della Pietra, A., 3rd, et al. (2012). EZH2 inhibition as a therapeutic strategy for lymphoma with EZH2-activating mutations. *Nature* 492, 108–112.
- McGrath, J.P., Williamson, K.E., Balasubramanian, S., Odate, S., Arora, S., Hatton, C., Edwards, T.M., O'Brien, T., Magnuson, S., Stokoe, D., et al. (2016). Pharmacological inhibition of the histone lysine demethylase KDM1A suppresses the growth of multiple acute myeloid leukemia subtypes. *Cancer Res.* 76, 1975–1988.
- Mitchell, L.H., Drew, A.E., Ribich, S.A., Rioux, N., Swinger, K.K., Jacques, S.L., Lingaraj, T., Boriack-Sjodin, P.A., Waters, N.J., Wigle, T.J., et al. (2015). Aryl pyrazoles as potent inhibitors of arginine methyltransferases: identification of the first PRMT6 tool compound. *ACS Med. Chem. Lett.* 6, 655–659.

- Nicholson, T.B., Chen, T., and Richard, S. (2009). The physiological and pathophysiological role of PRMT1-mediated protein arginine methylation. *Pharmacol. Res.* *60*, 466–474.
- Papasaikas, P., Tejedor, J.R., Vigevani, L., and Valcarcel, J. (2015). Functional splicing network reveals extensive regulatory potential of the core spliceosomal machinery. *Mol. Cell* *57*, 7–22.
- Pawlak, M.R., Scherer, C.A., Chen, J., Roshon, M.J., and Ruley, H.E. (2000). Arginine N-methyltransferase 1 is required for early postimplantation mouse development, but cells deficient in the enzyme are viable. *Mol. Cell. Biol.* *20*, 4859–4869.
- Ren, J., Wang, Y., Liang, Y., Zhang, Y., Bao, S., and Xu, Z. (2010). Methylation of ribosomal protein S10 by protein-arginine methyltransferase 5 regulates ribosome biogenesis. *J. Biol. Chem.* *285*, 12695–12705.
- Shailesh, H., Zakaria, Z.Z., Baiocchi, R., and Sif, S. (2018). Protein arginine methyltransferase 5 (PRMT5) dysregulation in cancer. *Oncotarget* *9*, 36705–36718.
- Shen, S., Park, J.W., Lu, Z.X., Lin, L., Henry, M.D., Wu, Y.N., Zhou, Q., and Xing, Y. (2014). rMATS: robust and flexible detection of differential alternative splicing from replicate RNA-seq data. *Proc. Natl. Acad. Sci. U S A* *111*, E5593–E5601.
- Shia, W.J., Okumura, A.J., Yan, M., Sarkeshik, A., Lo, M.C., Matsuura, S., Komeno, Y., Zhao, X., Nimer, S.D., Yates, J.R., 3rd, and Zhang, D.E. (2012). PRMT1 interacts with AML1-ETO to promote its transcriptional activation and progenitor cell proliferative potential. *Blood* *119*, 4953–4962.
- Smil, D., Eram, M.S., Li, F., Kennedy, S., Szewczyk, M.M., Brown, P.J., Barsyte-Lovejoy, D., Arrowsmith, C.H., Vedadi, M., and Schapira, M. (2015). Discovery of a dual PRMT5-PRMT7 inhibitor. *ACS Med. Chem. Lett.* *6*, 408–412.
- Stokes, M.P., Farnsworth, C.L., Moritz, A., Silva, J.C., Jia, X., Lee, K.A., Guo, A., Polakiewicz, R.D., and Comb, M.J. (2012). PTMScan direct: identification and quantification of peptides from critical signaling proteins by immunoaffinity enrichment coupled with LC-MS/MS. *Mol. Cell. Proteomics* *11*, 187–201.
- Stopa, N., Krebs, J.E., and Shechter, D. (2015). The PRMT5 arginine methyltransferase: many roles in development, cancer and beyond. *Cell. Mol. Life Sci.* *72*, 2041–2059.
- Takai, H., Masuda, K., Sato, T., Sakaguchi, Y., Suzuki, T., Suzuki, T., Koyama-Nasu, R., Nasu-Nishimura, Y., Katou, Y., Ogawa, H., et al. (2014). 5-Hydroxymethylcytosine plays a critical role in glioblastomagenesis by recruiting the CHTOP-methylosome complex. *Cell Rep.* *9*, 48–60.
- Veland, N., Hardikar, S., Zhong, Y., Gayatri, S., Dan, J., Strahl, B.D., Rothbart, S.B., Bedford, M.T., and Chen, T. (2017). The arginine methyltransferase PRMT6 regulates DNA methylation and contributes to global DNA hypomethylation in cancer. *Cell Rep.* *21*, 3390–3397.
- Wall, M.L., and Lewis, S.M. (2017). Methylarginines within the RGG-motif region of hnRNP A1 affect its IRES trans-acting factor activity and are required for hnRNP A1 stress granule localization and formation. *J. Mol. Biol.* *429*, 295–307.
- Wang, L., Nie, J., Sicotte, H., Li, Y., Eckel-Passow, J.E., Dasari, S., Vedell, P.T., Barman, P., Wang, L., Weinshiboum, R., et al. (2016). Measure transcript integrity using RNA-seq data. *BMC Bioinformatics* *17*, 58.
- Wang, L., Wang, S., and Li, W. (2012). RSeQC: quality control of RNA-seq experiments. *Bioinformatics* *28*, 2184–2185.
- Wang, L., Zhao, Z., Meyer, M.B., Saha, S., Yu, M., Guo, A., Wisinski, K.B., Huang, W., Cai, W., Pike, J.W., et al. (2014). CARM1 methylates chromatin remodeling factor BAF155 to enhance tumor progression and metastasis. *Cancer Cell* *25*, 21–36.
- Wang, Y., Xiao, X., Zhang, J., Choudhury, R., Robertson, A., Li, K., Ma, M., Burge, C.B., and Wang, Z. (2013). A complex network of factors with overlapping affinities represses splicing through intronic elements. *Nat. Struct. Mol. Biol.* *20*, 36–45.
- Wei, H., Mundade, R., Lange, K.C., and Lu, T. (2014). Protein arginine methylation of non-histone proteins and its role in diseases. *Cell Cycle* *13*, 32–41.
- Yang, Y., and Bedford, M.T. (2013). Protein arginine methyltransferases and cancer. *Nat. Rev. Cancer* *13*, 37–50.
- Yoshimatsu, M., Toyokawa, G., Hayami, S., Unoki, M., Tsunoda, T., Field, H.I., Kelly, J.D., Neal, D.E., Maehara, Y., Ponder, B.A., et al. (2011). Dysregulation of PRMT1 and PRMT6, type I arginine methyltransferases, is involved in various types of human cancers. *Int. J. Cancer* *128*, 562–573.
- Zhao, X., Jankovic, V., Gural, A., Huang, G., Pardanani, A., Menendez, S., Zhang, J., Dunne, R., Xiao, A., Erdjument-Bromage, H., et al. (2008). Methylation of RUNX1 by PRMT1 abrogates SIN3A binding and potentiates its transcriptional activity. *Genes Dev.* *22*, 640–653.
- Zheng, S., Moehlenbrink, J., Lu, Y.C., Zalmas, L.P., Sagum, C.A., Carr, S., McGouran, J.F., Alexander, L., Fedorov, O., Munro, S., et al. (2013). Arginine methylation-dependent reader-writer interplay governs growth control by E2F-1. *Mol. Cell* *52*, 37–51.

STAR★METHODS

KEY RESOURCES TABLE

REAGENT or RESOURCE	SOURCE	IDENTIFIER
Antibodies		
rabbit anti-mono-methyl Arginine (MMA)	Cell Signalling	Cat# 8711; RRID: AB_10896849
rabbit anti-symmetric-di-methyl Arginine (SDMA)	Cell Signalling	Cat# 13222S, clone D2C3D6; RRID: AB_2714013
rabbit anti-asymmetric dimethyl Arginine (ADMA)	Cell Signalling	Cat# 13522S; RRID: AB_2665370
rabbit-anti MTAP	Cell Signalling	Cat# 4158S; RRID: AB_1904054
rabbit-anti KHRDBS1/SAM68	Bethyl	Cat# A302-110A; RRID: AB_1604287
mouse anti- α -tubulin	Sigma	Cat# T9026; RRID: AB_477593
mouse anti- α -actin	Sigma	Cat# A2228; RRID: AB_476697
IRDye 800CW goat anti-Rabbit IgG (H+L)	LiCor	Cat# 926-32211; RRID: AB_621843
and IRDye 680RD goat anti-mouse IgG (H+L)	LiCor	Cat# 926-68070; RRID: AB_10956588
Critical Commercial Assays		
CellTiter-Glo One Solution Assay	Promega	Cat# G8462
Caspase-Glo® 3/7 Assay	Promega	Cat# G811B
CycleTEST PLUS DNA Reagent Kit	Becton Dickinson	Cat# 340242
High capacity cDNA kit	Applied Biosystems	Cat# 4368814
Fast taq man master mix	Applied Biosystems	Cat# 4444554
Pierce Classic Magnetic IP/Co-IP Kit	Pierce	Cat# 88805
TruSeq Stranded mRNA sample preparation kit	Illumina	Cat# RS-122-2103
QIAshredder column	QIAGEN	Cat# 79656
1X RIPA	Sigma	Cat# R0278
Protease/Phosphatase inhibitor cocktail	Cell Signalling	Cat# 5872
BCA Protein Assay	Pierce	Cat# 232778, 1859078
NuPAGE LDS Sample Buffer	Life Technologies	Cat# NP0007
NuPAGE Reducing Agent	Life Technologies	Cat# NP0004
MES Running Buffer	Life Technologies	Cat# NP0002
NuPAGE Novex 4-12% Bis-Tris gels	Life Technologies	Cat# NPO323BOX, NPO336BOX
iBLOT2 NC Regular Stacks	Invitrogen	Cat# IB23001
Blocking Buffer	LiCor	Cat# 927-40000
Deposited Data		
RNA-seq data	This paper	GEO: GSE126651
Crystal structure of GSK3368715 with PRMT1	This paper	PDB; 6NT2
Methylscan data	This paper	PXD012747
Experimental Models: Cell Lines		
See Table S8		
Oligonucleotides		
MTAP exon 1 crRNA (ccgtgaaggtgagatgagcc)	GE Healthcare/Dharmacon	Cat# CM-009539-02-0010
Non-targeting control crRNA	GE Healthcare/Dharmacon	Cat# U-007505-20
Edit-R Cas9 Nuclease protein NLS, 20 micromolar	GE Healthcare/Dharmacon	Cat# CAS11201
POP4 exons 2-3	Applied Biosystems	Hs01573980_m1
POP4 exons 2-4, skipped 3	Applied Biosystems	Hs03679234_m1
POP4 exons 3-4	Applied Biosystems	Hs00198357_m1
POP4 exons 4-5	Applied Biosystems	Hs01592578_m1
NUPL2 exons 2-4, skipped 3	Applied Biosystems	Hs01032729_m1
NUPL2 exons 2-3	Applied Biosystems	Hs01032732_m1

(Continued on next page)

Continued

REAGENT or RESOURCE	SOURCE	IDENTIFIER
NUPL2 exons 3-4	Applied Biosystems	Hs01032733_m1
NUPL2 exons 6-7	Applied Biosystems	Hs01032731_m1
SLC9B2 exons 5-3, skipped 4	Applied Biosystems	Hs01104999_m1
SLC9B2 exons 5-4	Applied Biosystems	Hs01104995_m1
SLC9B2 exons 4-3	Applied Biosystems	Hs01104994_m1
SLC9B2 exons 10-9	Applied Biosystems	Hs01104990_m1
PPM1M exons 2-4, skipped 3	Applied Biosystems	Hs00293388_m1
PPM1M exons 2-3	Applied Biosystems	Hs00997004_g1
PPM1M exons 3-4	Applied Biosystems	Hs00376140_m1
PPM1M exons 9-10	Applied Biosystems	Hs00997010_g1
ENFA1 exons 2-4, skipped 3	Applied Biosystems	Hs01020895_m1
ENFA1 exons 2-3	Applied Biosystems	Hs00358887_m1
ENFA1 exons 3-4	Applied Biosystems	Hs01014370_g1
ENFA1 exons 1-2	Applied Biosystems	Hs00358886_m1
MKI67 exons 8-6, skipped 7	Applied Biosystems	Hs00267195_m1
MKI67 exons 8-7	Applied Biosystems	Hs01032442_m1
MKI67 exons 7-6	Applied Biosystems	Hs01032441_g1
MKI67 exons 12-11	Applied Biosystems	Hs01032434_m1
IGSF3 exons 4-6 skipped 5	Applied Biosystems	Hs01035588_m1
IGSF3 exons 4-5	Applied Biosystems	Hs01035594_m1
IGSF3 exons 5-6	Applied Biosystems	Hs01035593_m1
IGSF3 exons 1-2	Applied Biosystems	Hs01035583_m1
ZFP62 exons 1-2	Applied Biosystems	Hs04189955_g1
ZFP62 exons 2-3	Applied Biosystems	Hs04189954_m1
ZFP62 exons 1-3, skipped 2	Applied Biosystems	Hs04187076_m1
ZFP62 exons 1	Applied Biosystems	Hs01930625_s1
OARD1 exons 6-5	Applied Biosystems	Hs01042865_m1
OARD1 exons 5-4	Applied Biosystems	Hs01042864_m1
OARD1 exons 6-4, skipped 5	Applied Biosystems	Hs01046363_m1
OARD1 exons 4-3	Applied Biosystems	Hs01042863_m1
GRB7 exons 12-13	Applied Biosystems	Hs00918001_g1
GRB7 exons 13-14	Applied Biosystems	Hs00918002_g1
GRB7 exons 12-14 skipped 13	Applied Biosystems	Hs00919114_g1
GRB7 exons 10-11	Applied Biosystems	Hs00917999_g1

CONTACT FOR REAGENT AND RESOURCE SHARING

Further information and requests for resources and reagents should be directed to and will be fulfilled by the Lead Contact, Helai Mohammad (helai.x.mohammad@gsk.com).

EXPERIMENTAL MODELS AND SUBJECT DETAILS**Tumor Growth Assessment of Human Tumor Xenografts**

For cell line xenografts, a single cell suspension of Toledo, BxPC3, MiaPaca-2, ACHN, or MDA-MB-468 cells was created in 100% Matrigel, containing 4-8 million cells, and delivered subcutaneously in the rear flank. Once tumor growth was evident, tumor volume and body weights were measured twice weekly. Tumor volumes were calculated based on the formula: tumor volume = (Length x Width²)/2. Following randomization into study groups (n = 10 per group) when the mean tumor size reached ~150-250 mm³, animals were dosed as indicated in each study. Animals were monitored daily and any clinical observations were recorded immediately. The percentage of tumor volume growth inhibition (TGI) was calculated on the final day with a complete vehicle group, using the following formula:

$$1 - \left[\frac{\text{average growth of the drug treated population Day last} - \text{average growth of the drug treated population Day 0}}{\text{average growth of the vehicle treated control population on Day last} - \text{average growth of the vehicle treated control population on Day 0}} \right] * 100.$$

Student's t-test was used to determine statistical significance between compound and vehicle treated groups.

Efficacy studies of GSK3368712 in a pancreatic patient derived xenograft model (PAXF 2076) were carried out at Charles River Discovery Research Services Germany (Freiburg, Germany). Tumor fragments were implanted into Female NMRI nu/nu mice (NMRI-*Foxn1^{nu}*). Animals and tumor implants were monitored daily until solid tumor growth was detectable in a sufficient number of animals. Following randomization, animals were assigned into study groups and dosed once daily with vehicle or GSK3368712.

All human biological samples were sourced ethically and their research use was in accord with the terms of the informed consents. The use of human tissue samples was reviewed and approved by GSK Research & Development Compliance (RDC) Human Biological Sample Use Committee. The human biological samples were sourced ethically and their research use was in accord with the terms of the informed consents under an IRB/EC approved protocol. All studies were conducted in accordance with the GSK Policy on the Care, Welfare and Treatment of Laboratory Animals and were reviewed by the Institutional Animal Care and Use Committee at GSK as well as by the ethical review process at Charles River or Frontage laboratories if the work was performed outside GSK.

Toxicology Assessment

The toxicological profile of once-daily, oral dosing of GSK3368715 was evaluated in rising and repeat dose toxicity studies (GSK Pharmaceuticals). Doses up to the maximal tolerated dose were evaluated in dose range studies. Studies were conducted using pharmacologically relevant rodent (rat; 10-12 week old Wistar:Han; n=10-16 per sex per group) and non-rodent (dog; 10-12 month old beagle; n=3-5 per sex per group) species. Assessments were GLP compliant and consistent with ICH S9 guidance. All studies were conducted in accordance with the GSK Policy on the Care, Welfare and Treatment of Laboratory Animals and were reviewed by the Institutional Animal Care and Use Committee at GSK.

DLBCL Colony Formation Assays

GSK3368715 was evaluated at 20, 5, 1.25, 0.3125 and 0.078 μ M in a total of 10 patient samples. DLBCL patient cells from 10 unique donors were received as frozen samples from Conversant Bio. The human biological samples were sourced ethically and their research use was in accord with the terms of the informed consents under an IRB/EC approved protocol. The use of human tissue samples was reviewed and approved by GSK Research & Development Compliance (RDC) Human Biological Sample Use Committee. Samples were thawed rapidly and diluted in 10 ml of IMDM + 10% FBS and washed. The supernatant was discarded and the cell pellets were resuspended in a known volume of IMDM + 10% FBS. To assess the effect of the test compound on DLBCL CFC, a methylcellulose media formulation containing 10% ALCM was used. The cultures were incubated in a humidified incubator at 37°C, 5% CO₂ for 14 days and the colonies then manually enumerated.

Cell Lines

Cell lines were obtained from various repositories and licensed accordingly. All cell lines were maintained in the recommended cell culture media at 37°C in 5% CO₂. Identity of all cell lines was validated by STR profiling, and each cell line was confirmed negative for mycoplasma.

Generation of *MTAP*-Deficient Clones

The first exon of *MTAP* was targeted by introduction of a guide crRNA (GE Healthcare/Dharmacon) and Cas9 protein (GE Healthcare/Dharmacon) by nucleofection following manufacturers instructions (Lonza). Following isolation and expansion of single cell clones, mutation in the first exon was determined by sequencing, and effect on MTAP protein verified by Western Blot (rabbit-anti MTAP 4158S, Cell Signaling Technology; mouse anti Actin A2228, Sigma). Three independent clones with homozygous loss of *MTAP*, one with heterozygous mutation, and one where targeting was unsuccessful, were chosen for further study.

METHOD DETAILS

Synthesis of GSK3368715

Abbreviations	
aq	aqueous
BINAP	2,2'-bis(diphenylphosphino) -1,1'-binaphthyl
(Boc) ₂ O	di- <i>tert</i> -butyl dicarbonate
ca	circa
CDCl ₃ - <i>d</i>	chloroform- <i>d</i>
CD ₃ OD- <i>d</i> 4	methanol- <i>d</i> 4
Cs ₂ CO ₃	cesium carbonate
CHCl ₃	chloroform
CH ₃ CN, ACN	acetonitrile

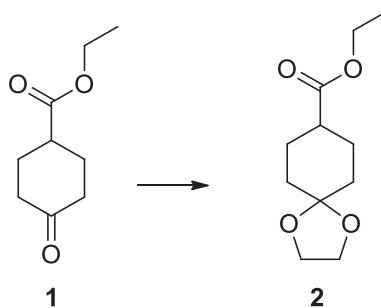
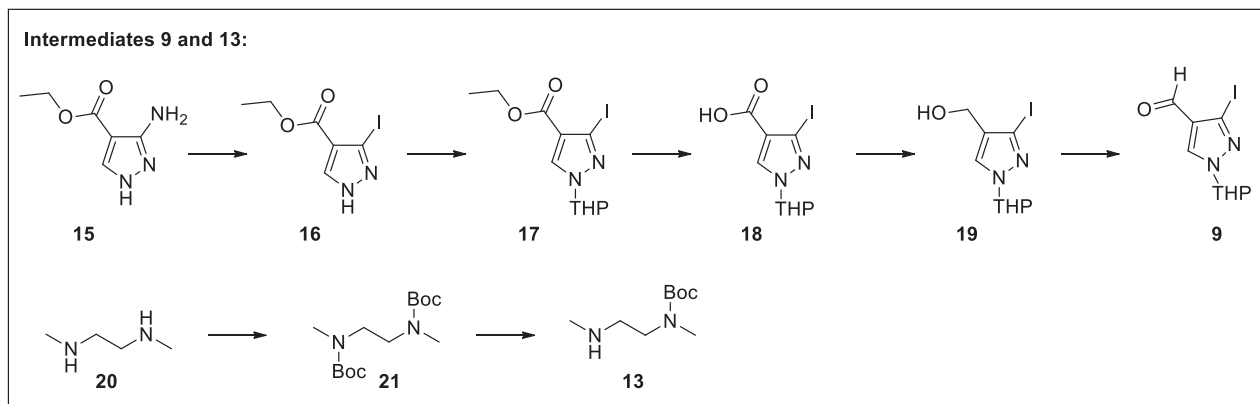
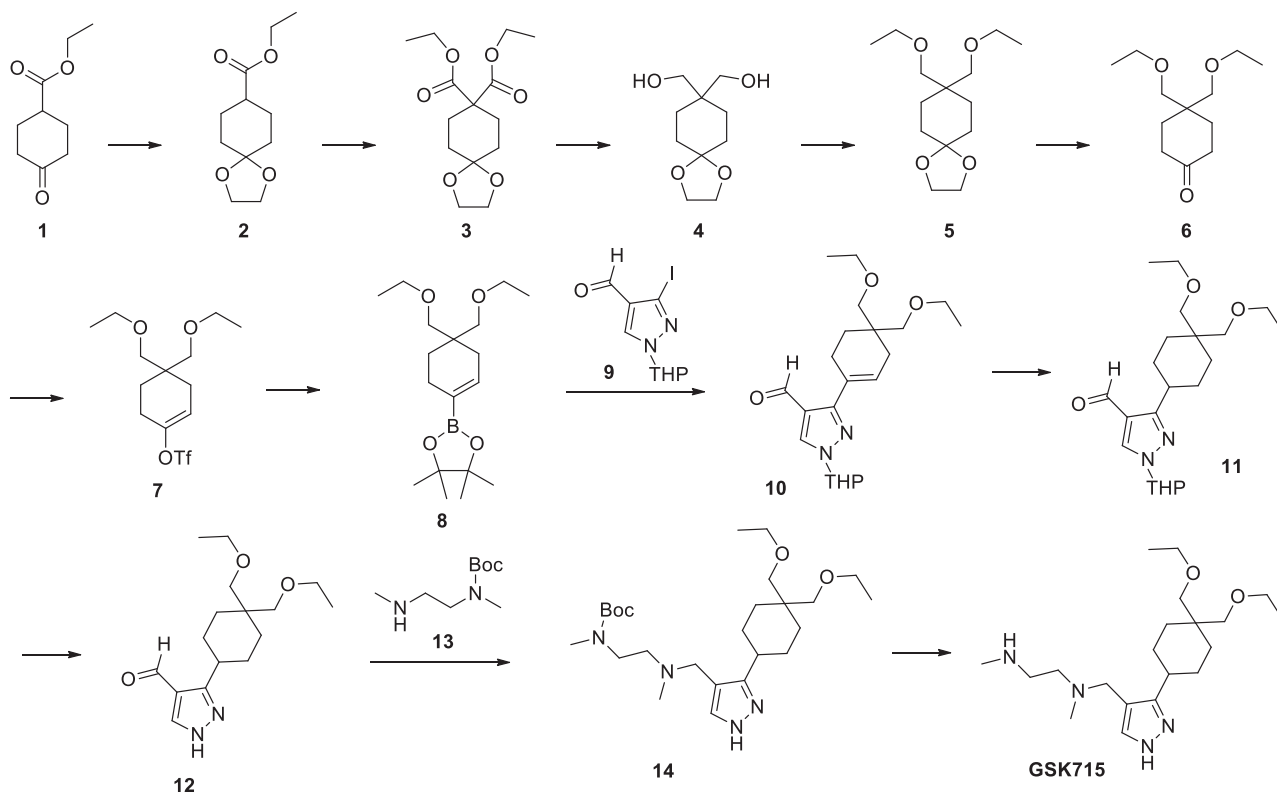
(Continued on next page)

Continued

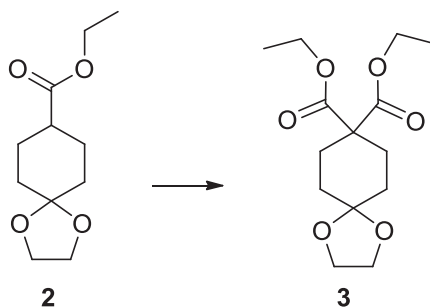
Abbreviations

Celite®	registered trademark of Celite Corp. brand of diatomaceous earth
DBU	1,8-diazabicyclo[5.4.0]undeca-7-ene
DCE	dichloroethane
DCM	methylene chloride
DME	1,2 dimethoxyethane
DMF	N,N-dimethylformamide
DIEA	diisopropyl ethylamine
DMSO- <i>d</i> 6	dimethylsulfoxide- <i>d</i> 6
EtOAc	ethyl acetate
EDC	1-(3-dimethylaminopropyl)-3-ethylcarbodiimide hydrochloride
FeCl ₃	iron trichloride
h	hour(s)
HCl	hydrogen chloride
¹ H NMR	proton nuclear magnetic resonance
HCl	hydrochloric acid
HOAT	1-hydroxy-7-azabenzotriazole
HPLC	high performance liquid chromatography
IPA	2-propanol
K ₂ CO ₃	potassium carbonate
KOH	potassium hydroxide
KI	potassium iodide
LC/MS	liquid chromatography/mass spectroscopy
LiHMDS	lithium bis(trimethylsilyl)amide
MgSO ₄	magnesium sulfate
MeOH	methanol
min	minute(s)
MTBE	methyl tert-butyl ether
MS	mass spectrometry
n-BuLi	n-butyl lithium
NaBH ₄	sodium borohydride
NaCl	sodium chloride
NaOH	sodium hydroxide
Na ₂ SO ₄	sodium sulfate
NH ₄ Cl	ammonium chloride
NH ₄ OH	ammonium hydroxide
NMM	4-methylmorpholine
NMP	N-Methyl-2-pyrrolidone
Pd/C	Palladium (10% by wt) on carbon
PdCl ₂ (dppf)	1,1'-Bis(diphenylphosphino)ferrocene-palladium(II)dichloride
Pd(Ph ₃ P) ₄	tetrakis(triphenylphosphine)palladium(0)
PE	petroleum ether
PhNMe ₂	N,N-dimethylaniline
RT	room temperature
SOCl ₂	thionyl chloride
SPhos	2-Dicyclohexylphosphino-2',6'-dimethoxybiphenyl
TFA	trifluoroacetic acid
THF	tetrahydrofuran
TLC	thin layer chromatography
ZnCl ₂	zinc chloride

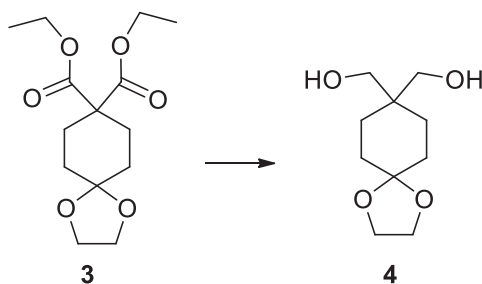
Intermediates were characterized by LCMS and/or ^1H NMR to confirm the structures and purity and carried to the next step without further purification unless otherwise noted. The synthetic scheme of GSK715 and preparation of indicated intermediates is described below.



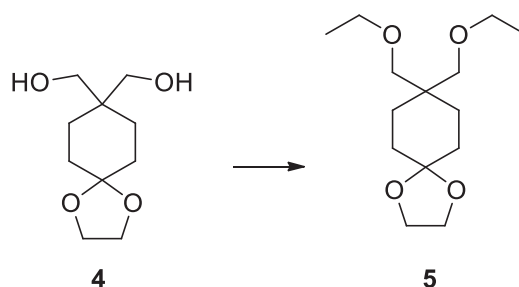
ethyl 1,4-dioxaspiro[4.5]decane-8-carboxylate (2). To a 20-L 4-necked round-bottom flask were added ethyl 4-oxocyclohexane-1-carboxylate (1 kg, 5.88 mol, 1.00 equiv), cyclohexane (10 L), ethane-1,2-diol (401 g, 6.46 mol, 1.10 equiv), *p*-TsOH (50 g, 0.3 mol, 0.05 eq). The resulting solution was stirred for 36 h at 80°C. The water generated from the reaction system was separated by water segregator. The resulting mixture was concentrated under vacuum. The resulting residue was diluted with 5 L of EA. The resulting mixture was washed with 3x4 L of saturated sodium bicarbonate. The resulting mixture was washed with 2x4 L of brine. The mixture was dried over anhydrous sodium sulfate, filtered and concentrated under vacuum to afford 1.1 kg (crude) of ethyl 1,4-dioxaspiro[4.5]decane-8-carboxylate as a yellow oil. The reaction was repeated 8 times and 8.8 kg (82% purity in GC/MS) of ethyl 1,4-dioxaspiro[4.5]decane-8-carboxylate (2) was obtained, which was used in the next step without further purification. ¹H NMR (300 MHz, Chloroform-*d*) δ 4.11 (q, *J* = 7.1 Hz, 2H), 3.93 (s, 4H), 2.41 – 2.21 (m, 1H), 2.01 – 1.68 (m, 6H), 1.66 – 1.45 (m, 2H), 1.23 (t, *J* = 7.1 Hz, 3H).



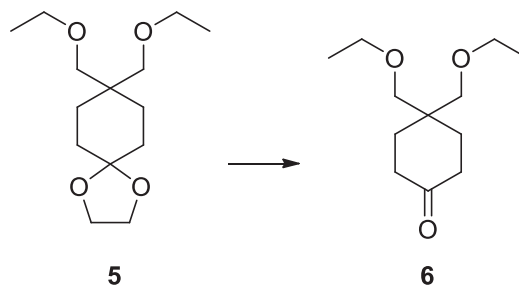
8,8-diethyl 1,4-dioxaspiro[4.5]decane-8,8-dicarboxylate (3). Into a 20-L 4-necked round-bottom flask purged and maintained with an inert atmosphere of nitrogen, was placed ethyl 1,4-dioxaspiro[4.5]decane-8-carboxylate (800 g, 3.73 mol, 1.00 equiv) and THF (8 L). The mixture was cooled to –78°C and LDA (3 L, 2M) was added dropwise with stirring at over 40 min. The resulting solution was stirred for 30 min at –40°C. To this was added catalytic chloride (484 g, 4.46 mol, 1.19 equiv) dropwise with stirring at –78°C over 30 min. The resulting solution was stirred for 1 h at –78°C and warmed naturally to room temperature and stirred overnight. The reaction was quenched by the addition of 2 L of NH₄Cl (saturated). The resulting mixture was concentrated under vacuum. The resulting solution was extracted with 3x2 L of ethyl acetate. The organic layers were combined and dried over anhydrous sodium sulfate, filtered and concentrated under vacuum. The residue was purified by silica gel chromatography using ethyl acetate/petroleum ether (1:20). This resulted in 550 g (51%) of 8,8-diethyl 1,4-dioxaspiro[4.5]decane-8,8-dicarboxylate (3) as yellow oil. The reaction was repeated 11 times and 6 kg of product was obtained. ¹H NMR (300 MHz, DMSO-*d*6) δ 4.15 (q, *J* = 7.1 Hz, 4H), 3.89 (s, 4H), 2.15 – 1.92 (m, 4H), 1.68 – 1.46 (m, 4H), 1.18 (t, *J* = 7.1 Hz, 6H).



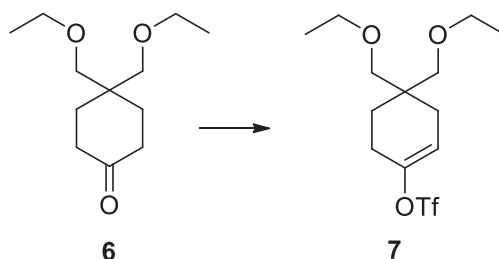
[8-(hydroxymethyl)-1,4-dioxaspiro[4.5]decan-8-yl]methanol (4). Into a 20L 4-necked round-bottom flask purged and maintained with an inert atmosphere of nitrogen, was placed THF (5.7 L) and dichlorozinc (542 g, 3.98 mol, 2.00 equiv). Sodium borohydride (379 g, 10.29 mol, 5.17 equiv) was added to the mixture portionwise at 0–5°C over 5 min with stirring. To this mixture was added 8,8-diethyl 1,4-dioxaspiro[4.5]decane-8,8-dicarboxylate (570 g, 1.99 mol, 1.00 equiv) with stirring at 0°C over 10 min. To the mixture was added triethylamine (202 g, 2.00 mol, 1.00 equiv) dropwise with stirring at 0°C in 15 min. The resulting solution was stirred for 4 h at 80°C. The reaction was then quenched by the addition of 5 L of NH₄Cl (saturated aqueous) then stirred for 2 h. The solution was extracted with 5x3 L of THF. The organic layer combined and concentrated under high vacuum. This resulted in 286 g (71%) of [8-(hydroxymethyl)-1,4-dioxaspiro[4.5]decan-8-yl]methanol (4) as a white solid. This reaction was repeated 10 times and 2800 g of product obtained. ¹H NMR (300 MHz, Methanol-*d*4) δ 3.93 (s, 4H), 3.49 (s, 4H), 1.65 – 1.58 (m, 4H), 1.55 – 1.48 (m, 4H).



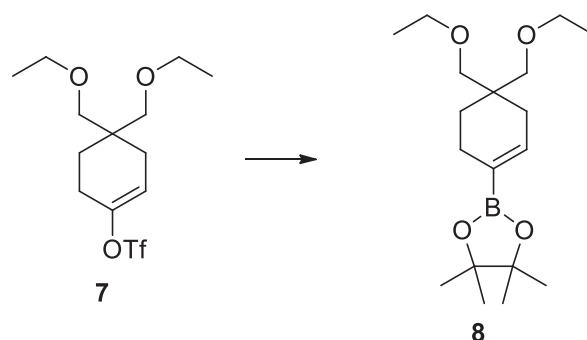
8,8-bis(ethoxymethyl)-1,4-dioxaspiro[4.5]decane (5). Into a 20-L 4-necked round-bottom flask, was placed [8-(hydroxymethyl)-1,4-dioxaspiro[4.5]decan-8-yl]methanol (970 g, 4.80 mol, 1.00 equiv), DMSO (5 L), water (5 L), KOH (1613 g, 28.75 mol, 5.99 equiv) and iodoethane (3745 g, 24.01 mol, 5.01 equiv). The resulting solution was stirred overnight at room temperature. The resulting solution was diluted with 20 L of H₂O. The resulting solution was extracted with 2x5 L of ethyl acetate and the organic layers combined and concentrated under vacuum. The residue was purified by silica gel chromatography using ethyl acetate/petroleum ether (1:50) to provide 920 g of 8,8-bis(ethoxymethyl)-1,4-dioxaspiro[4.5]decane (5) as a yellow oil. ¹H NMR (300 MHz, Chloroform-*d*) δ 3.97 (s, 4H), 3.49 (q, *J* = 7.0 Hz, 4H), 3.32 (s, 4H), 1.63–1.58 (m, 4H), 1.45–1.00 (m, 4H), 0.89–0.81 (m, 6H).



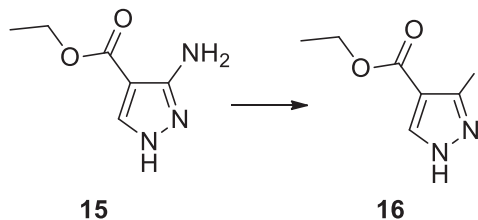
4,4-bis(ethoxymethyl)cyclohexan-1-one (6). Into a 20-L 3-necked round-bottom flask, was placed 8,8-bis(ethoxymethyl)-1,4-dioxaspiro[4.5]decane (920 g, 3.56 mol, 1.00 equiv), dichloromethane (10 L) and FeCl₃·6H₂O (3357 g). The resulting solution was stirred overnight at room temperature. The solids were filtered out. The resulting solution was diluted with 10 L of DCM. The resulting mixture was washed with 2x5 L of brine. The resulting mixture was concentrated under vacuum to provide 715 g of 4,4-bis(ethoxymethyl)cyclohexan-1-one (6) as yellow oil. This reaction was repeated 2 times and 1430 g of product obtained. ¹H NMR (300 MHz, Chloroform-*d*) δ 3.50 (q, *J* = 7.0 Hz, 4H), 3.38 (s, 4H), 2.37 (t, *J* = 7.0 Hz, 4H), 1.80 (t, *J* = 6.9 Hz, 4H), 1.19 (t, *J* = 6.9 Hz, 6H).



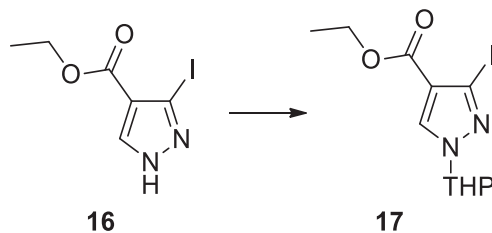
4,4-bis(ethoxymethyl)cyclohex-1-en-1-yl trifluoromethanesulfonate (7). Into a 10-L 4-necked round-bottom flask purged and maintained with an inert atmosphere of nitrogen, was placed 4,4-bis(ethoxymethyl)cyclohexan-1-one (300 g, 1.40 mol, 1.00 equiv) and THF (3 L). The mixture was cooled to -78°C and LiHMDS (1682 mL, 1 mol/L in THF) was added dropwise with stirring over 20 min. The mixture was stirred 0.5 h at -50°C . To this mixture was added 1,1,1-trifluoro-*N*-phenyl-*N*-(trifluoromethane)sulfonylmethanesulfonamide (525 g, 1.47 mol, 1.05 equiv), in portions at -78°C over 10 min. The resulting solution was warmed naturally to room temperature and stirred for 1 h. The reaction was then quenched by the addition of 1 L of water. The resulting solution was extracted with 2x2 L of ethyl acetate and the organic layers combined. The resulting mixture was washed with 2x2 L of brine. The resulting mixture was concentrated under vacuum. The residue was purified by silica gel chromatography using ethyl acetate/petroleum ether (1:50). This resulted in 380 g (78%) of 4,4-bis(ethoxymethyl)cyclohex-1-en-1-yl trifluoromethanesulfonate (7) as a yellow oil. This reaction was repeated 4 times and 1520 g of product obtained.



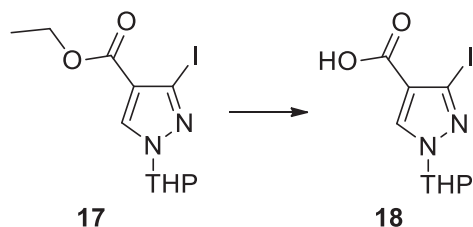
2-[4,4-bis(ethoxymethyl)cyclohex-1-en-1-yl]-4,4,5,5-tetrahydro-1,3,2-dioxaborolane (8). Into a 10-L 3-necked round-bottom flask purged and maintained with an inert atmosphere of nitrogen, was placed 4,4-bis(ethoxymethyl)cyclohex-1-en-1-yl trifluoromethanesulfonate (407 g, 1.18 mol, 1.00 equiv), 1,4-dioxane (4 L), 4,4,5,5-tetrahydro-2-(tetramethyl-1,3,2-dioxaborolan-2-yl)-1,3,2-dioxaborolane (269 g, 1.06 mol, 0.90 equiv), KOAc (346 g, 3.53 mol, 3.00 equiv) and Pd(dppf)Cl₂ (40 g, 54.67 mmol, 0.05 equiv). The resulting solution was stirred overnight at 80°C. The resulting solution was diluted with 5 L of EA. The resulting mixture was washed with 3x5 L of brine. The mixture was dried over anhydrous sodium sulfate, filtered and concentrated under vacuum. The residue was purified by silica gel chromatography using ethyl acetate/petroleum ether (1:50) to provide 325 g (85%) of 2-[4,4-bis(ethoxymethyl)cyclohex-1-en-1-yl]-4,4,5,5-tetrahydro-1,3,2-dioxaborolane (8) as a yellow oil. This reaction was repeated 4 times and 1300 g of product obtained. ¹H NMR (300 MHz, Chloroform-*d*) δ 6.51 (tt, *J* = 3.8, 1.9 Hz, 1H), 3.46 (q, *J* = 7.0 Hz, 4H), 3.26 (q, *J* = 9.0 Hz, 4H), 2.12 (tq, *J* = 6.3, 2.2 Hz, 2H), 1.99 (q, *J* = 2.8 Hz, 2H), 1.51 (t, *J* = 6.4 Hz, 2H), 1.28 (s, 12H), 1.17 (t, *J* = 7.0 Hz, 6H).



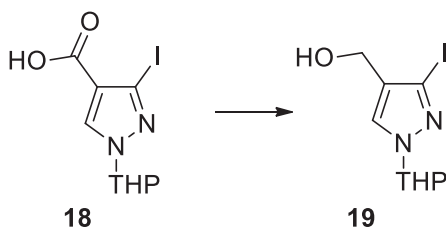
ethyl 3-iodo-1*H*-pyrazole-4-carboxylate (16). Into a 100-L vessel, ethyl 3-amino-1*H*-pyrazole-4-carboxylate (2 kg, 12.89 mol, 1.00 equiv) was dissolved in sulfuric acid (98%) (10 L) at 0°C, then ice water (10 L) was added at 0°C~5°C. To the mixture was added a solution of NaNO₂ (1088 g, 1.20 equiv) in water (5 L) dropwise with stirring at 0°C. The mixture was stirred for 1 h at 0°C~5°C. The mixture was added into a solution of KI (6.55 kg, 3.00 equiv) in water (15 L) at 0°C in another vessel. The resulting solution was stirred for 2 h at 0°C~5°C. The reaction mixture was extracted with ethyl acetate (10 Lx5), the organic layers was combined and washed with the saturated solution of Na₂CO₃ (10 Lx2) and Na₂SO₃ (10 Lx2). After concentrated, this resulted in 1.3 kg of ethyl 3-iodo-1*H*-pyrazole-4-carboxylate (16) as a yellow solid. The reaction was repeated 4 times and 5.1 kg of product obtained. LCMS(ES)+ *m/e* 267.0 [M+H]⁺.



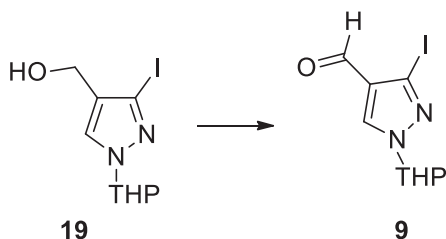
ethyl 3-iodo-1-(oxan-2-yl)-1*H*-pyrazole-4-carboxylate (17). To a 20-L 4-necked round-bottom flask purged and maintained with an inert atmosphere of nitrogen, were added a solution of ethyl 3-iodo-1*H*-pyrazole-4-carboxylate (1900 g, 7.14 mol, 1.00 equiv) in THF (10 L) and TsOH (123 g, 714 mmol, 0.10 equiv). To the mixture was added DHP (1800 g, 22.53 mol, 3.00 equiv) dropwise with stirring at 0°C. The resulting solution was stirred overnight at room temperature. The resulting mixture was concentrated under vacuum. The resulting solution was diluted with 5 L of ethyl acetate. The resulting mixture was washed with 3x5 L of brine. The mixture was dried over anhydrous sodium sulfate, filtered and concentrated under vacuum. The residue was purified by silica gel chromatography using ethyl acetate/petroleum ether (1:20-1:5) to provide 1.7 kg (68%) of ethyl 3-iodo-1-(oxan-2-yl)-1*H*-pyrazole-4-carboxylate (17) as a white solid. The reaction was repeated 3 times to provide 5.0 kg of the product. LCMS(ES)+ *m/e* 350.8 [M+H - THP]⁺.



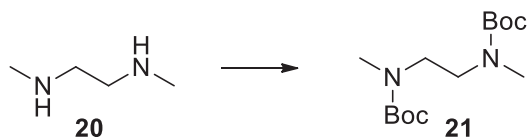
3-iodo-1-(tetrahydro-2*H*-pyran-2-yl)-1*H*-pyrazole-4-carboxylic acid (18). Into a 20-L 4-necked round-bottom flask, was placed a solution of ethyl 3-iodo-1-(oxan-2-yl)-1*H*-pyrazole-4-carboxylate (2.0 kg, 5.71 mol, 1.00 equiv) in tetrahydrofuran (4 L) and methanol (4 L). To the mixture was added a solution of LiOH (411 g, 17.16 mol, 3.00 equiv) in water (3 L) dropwise with stirring at 0°C. The resulting solution was stirred overnight at room temperature. The resulting mixture was concentrated under vacuum. The residue was diluted with 5 L of water. The pH value of the resulting solution was adjusted to 4-5 with HCl (1 mol/L) and extracted with 3x2 L of dichloromethane and the organic layers combined. The resulting mixture was washed with 3x3 L of brine. The mixture was dried over anhydrous sodium sulfate, filtered, and concentrated under vacuum. The resulted solids were suspended in 2L of hexane and stirred for 30 min then collected by filtration. The reaction was repeated 2 times to provide 2.5 kg of the product (18). LCMS(ES)⁺ m/e 323.0 [M+H]⁺.



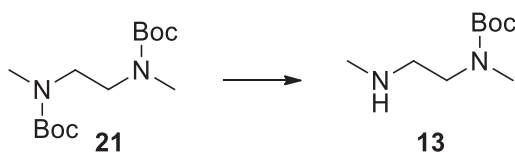
[3-iodo-1-(oxan-2-yl)-1*H*-pyrazol-4-yl]methanol (19). Into a 20-L 4-necked round-bottom flask purged and maintained with an inert atmosphere of nitrogen, was placed a solution of 3-iodo-1-(oxan-2-yl)-1*H*-pyrazole-4-carboxylic acid (1150 g, 3.57 mol, 1.00 equiv) in tetrahydrofuran (3 L). To the mixture was added a 1M solution of BH₃ in THF (7.1 L, 2.00 equiv) dropwise at 0°C. The resulting solution was stirred overnight at room temperature. The reaction was then quenched by addition 1 L of NH₄Cl (saturated aqueous). The resulting mixture was concentrated under vacuum. The resulting solution was extracted with 3x3 L of ethyl acetate and the organic layers combined. The resulting mixture was washed with 3x3 L of brine. The mixture was dried over anhydrous sodium sulfate, filtered, and concentrated under vacuum to provide 0.98 kg (89%) of [3-iodo-1-(oxan-2-yl)-1*H*-pyrazol-4-yl]methanol (19) as an off-white solid. The reaction was repeated 3 times to provide 2.9 kg of the product. LCMS(ES)⁺ m/e 309 [M+H]⁺.



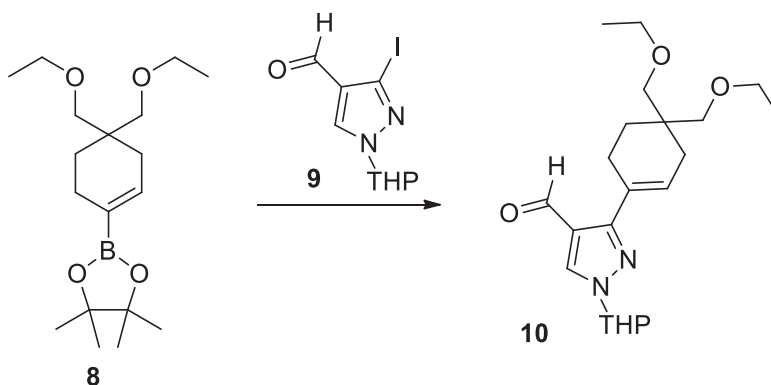
3-iodo-1-(oxan-2-yl)-1*H*-pyrazole-4-carbaldehyde (9). Into a 20-L 4-necked round-bottom flask, was placed a solution of [3-iodo-1-(oxan-2-yl)-1*H*-pyrazol-4-yl]methanol (1.5 kg, 4.87 mol, 1.00 equiv) in dichloromethane (10 L). MnO₂ (4236.9 g, 48.73 mol, 10.00 equiv) was added and the resulting mixture was stirred overnight at 50°C. The solids were filtered off and the filtrate was concentrated under vacuum. The resulting solid was suspended in a solution of EtOAc/pet ether (1:5, 1.5 L) and stirred for 2 h at RT. The solids were collected by filtration to provide 1.1 kg (74%) of 3-iodo-1-(oxan-2-yl)-1*H*-pyrazole-4-carbaldehyde (9) as a white solid. LCMS(ES)⁺ m/e 307.0 [M+H]⁺.



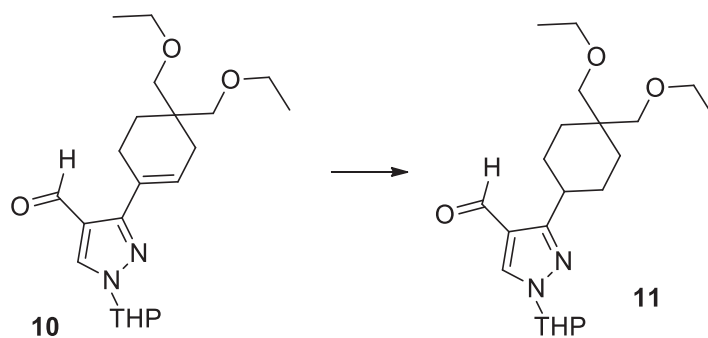
tert-butyl *N*-(2-[[tert-butoxy]carbonyl](methylamino)ethyl)-*N*-methylcarbamate (**21**). Into a 50-L 3-necked round-bottom flask purged and maintained with an inert atmosphere of nitrogen, was placed a solution of methyl[2-(methylamino)ethyl]amine (2.0 kg, 22.69 mol, 1.00 equiv) in dichloromethane (20 L). To the mixture was added a solution of Boc_2O (9.9 kg, 45.36 mol, 2.00 equiv) in dichloromethane (2 L) dropwise with stirring at 0°C. The resulting solution was stirred for 3 h at room temperature. The resulting mixture was concentrated under vacuum. The residue was diluted with 10 L of ethyl acetate and washed with 3x5 L of brine. The organics were dried over anhydrous sodium sulfate, filtered and concentrated under vacuum to provide 5.5 kg (84%) of tert-butyl *N*-(2-[[tert-butoxy]carbonyl](methylamino)ethyl)-*N*-methylcarbamate (**21**) as a white solid. ^1H NMR (300 MHz, DMSO-d_6) δ 3.27 (s, 4H), 2.77 (br s., 6H), 1.38 (s, 18H).



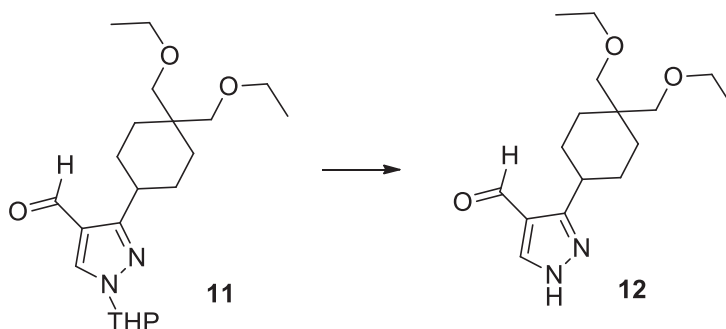
tert-butyl *N*-methyl-*N*-[2-(methylamino)ethyl]carbamate (**13**). Into a solution of tert-butyl *N*-(2-[[tert-butoxy]carbonyl](methylamino)ethyl)-*N*-methylcarbamate (5.5 kg, 19.1 mol) in methanol (30 L) was added AcCl (1.79 kg, 22.9 mol) dropwise with stirring at 0°C. The resulting solution was stirred overnight at room temperature. The mixture was concentrated under vacuum and the residue was diluted with EtOAc (20 L) and washed brine (3 x 20 L). The combined organics were dried over anhydrous sodium sulfate, filtered and concentrated under vacuum to provide 950 g (26%) of tert-butyl *N*-methyl-*N*-[2-(methylamino)ethyl]carbamate (**13**) as a yellow oil. ^1H NMR (400 MHz, DMSO-d_6) δ 3.19 (m, 2H), 2.77 (apparent br. s, 3H), 2.55 (m, 2H), 2.27 (s, 3H), 1.38 (s, 9H).



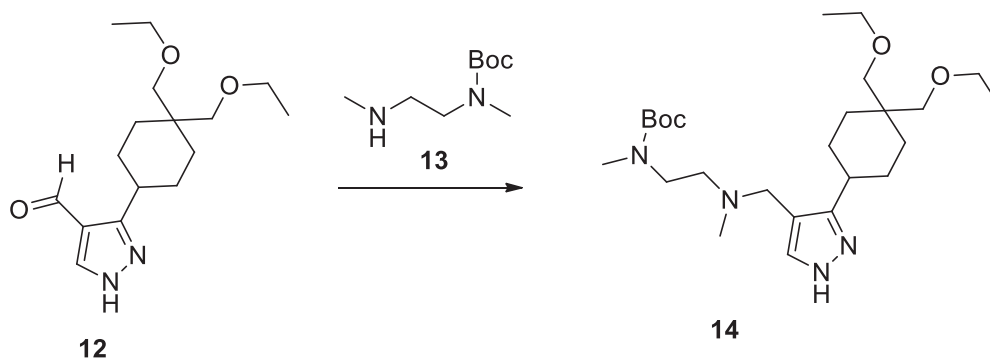
3-[4,4-bis(ethoxymethyl)cyclohex-1-en-1-yl]-1-(oxan-2-yl)-1H-pyrazole-4-carbaldehyde (**10**). Into a 10-L 3-necked round-bottom flask purged and maintained with an inert atmosphere of nitrogen, was placed 2-[4,4-bis(ethoxymethyl)cyclohex-1-en-1-yl]-4,4,5,5-tetramethyl-1,3,2-dioxaborolane (**8**, 318 g, 980.69 mmol, 1.00 equiv), 1,4-dioxane (3 L), 3-iodo-1-(oxan-2-yl)-1H-pyrazole-4-carbaldehyde (**9**, 270 g, 882.06 mmol, 0.90 equiv), water (300 mL), Cs_2CO_3 (960 g, 2.95 mol, 3.00 equiv) and $\text{Pd}(\text{dppf})\text{Cl}_2$ (30 g, 0.041 mol). The resulting mixture was stirred overnight at 100°C. The resulting solution was cooled to room temperature and diluted with 5 L of EtOAc. The resulting mixture was washed with 3x5 L of brine. The mixture was dried over anhydrous sodium sulfate, filtered and concentrated under vacuum. The residue was purified by silica gel chromatography using ethyl acetate/petroleum ether (1:20) to provide 210 g (57%) of 3-[4,4-bis(ethoxymethyl)cyclohex-1-en-1-yl]-1-(oxan-2-yl)-1H-pyrazole-4-carbaldehyde (**10**) as a yellow oil. This reaction was repeated 4 times to provide 820 g of product. LCMS(ES)⁺ m/e 377.1 $[\text{M}+\text{H}]^+$.



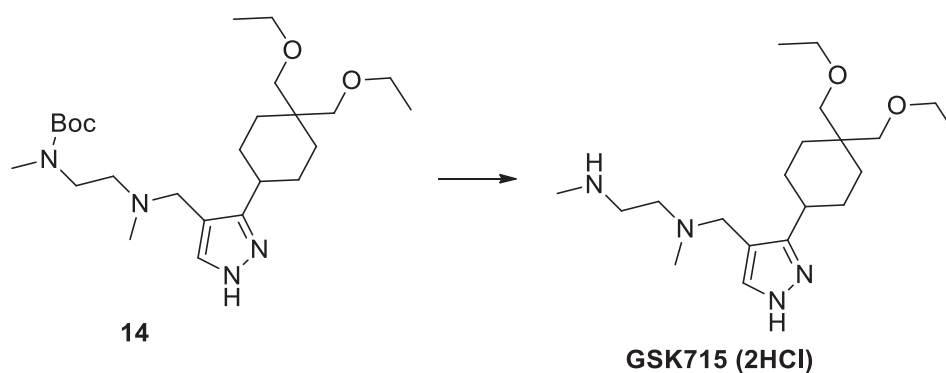
3-(4,4-bis(ethoxymethyl)cyclohexyl)-1-(tetrahydro-2H-pyran-2-yl)-1H-pyrazole-4-carbaldehyde (11). Into a 1000-mL round-bottom flask was placed 3-[4,4-bis(ethoxymethyl)cyclohex-1-en-1-yl]-1-(oxan-2-yl)-1H-pyrazole-4-carbaldehyde (50 g, 132.81 mmol, 1.00 equiv), tetrahydrofuran (500 mL) and palladium on carbon (10 g). The resulting mixture was stirred for 24 h at room temperature under hydrogen gas at atmospheric pressure. The solids were removed by filtration and the filtrate was concentrated under reduced pressure. The residue was purified by silica gel chromatography using ethyl acetate/petroleum ether (1:5) to afford 35 g (70%) of 3-(4,4-bis(ethoxymethyl)cyclohexyl)-1-(tetrahydro-2H-pyran-2-yl)-1H-pyrazole-4-carbaldehyde (11) as yellow oil. The reaction was repeated 16 times to provide 560 g of product. LCMS(ES)⁺ m/e 379.0 [M+H]⁺.



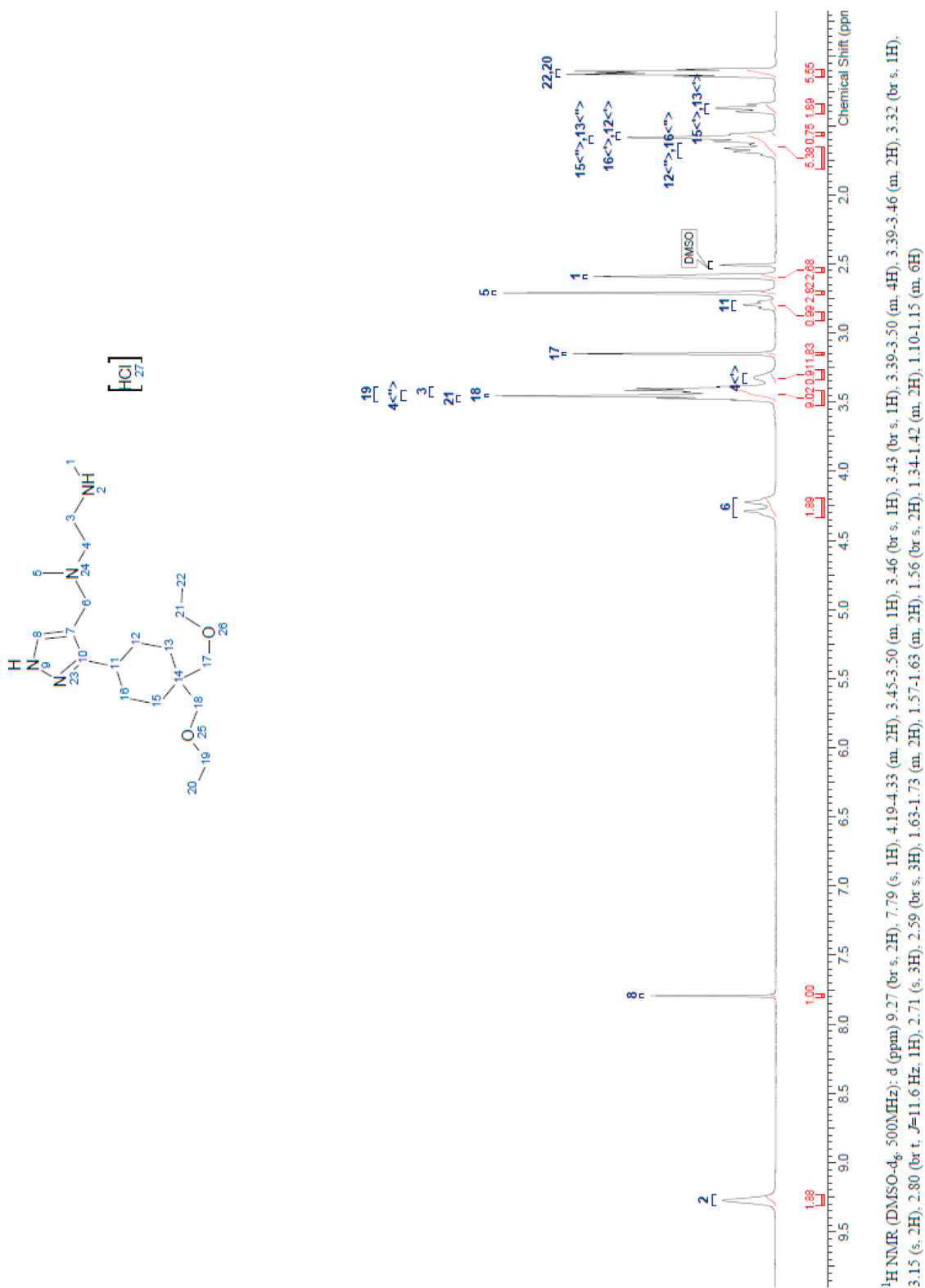
3-[4,4-bis(ethoxymethyl)cyclohexyl]-1H-pyrazole-4-carbaldehyde (12). Into a 10L 4-necked round-bottom flask was placed methanol (3 L), hydrogen chloride (3 L, 36%) and 3-[4,4-bis(ethoxymethyl)cyclohexyl]-1-(oxan-2-yl)-1H-pyrazole-4-carbaldehyde (560 g, 1.48 mol, 1.00 equiv). The resulting solution was stirred for 3 h at room temperature. The pH value of the solution was adjusted to 9 with aqueous sodium hydroxide (6 mol/L). The resulting solution was extracted with ethyl acetate (2 x 3 L) and the organic layers combined and concentrated under vacuum. The residue was purified by silica gel chromatography using ethyl acetate/petroleum ether (1:3) to provide 270 g (99% purity) and 150 g (95% purity) of 3-[4,4-bis(ethoxymethyl)cyclohexyl]-1H-pyrazole-4-carbaldehyde (12) as a yellow oil. LCMS(ES)⁺ m/e 295.0 [M+H]⁺.



tert-butyl *N*-[2-[[[3-[4,4-bis(ethoxymethyl)cyclohexyl]-1*H*-pyrazol-4-yl]methyl](methyl)amino]ethyl]-*N*-methylcarbamate (14). Into a 5-L 4-necked round-bottom flask purged and maintained with an inert atmosphere of nitrogen, was placed a solution of 3-[4,4-bis(ethoxymethyl)cyclohexyl]-1*H*-pyrazole-4-carbaldehyde (210 g, 713.34 mmol, 1.00 equiv) and tert-butyl *N*-methyl-*N*-[2-(methylamino)ethyl]carbamate (13, 201 g, 1.07 mol, 1.50 equiv) in dichloromethane (3L). Sodium triacetoxyborohydride (605 g, 2.857 mol, 4.00 equiv) was added in several batches with stirring over 2 h. The resulting solution was stirred for 12 h at room temperature. The reaction was then quenched by the addition of water. The resulting solution was extracted with 3x2 L of dichloromethane and the organic layers combined and concentrated under vacuum. The residue was purified by silica gel chromatography using dichloromethane/methanol (100:1 to 10:1) to afford 300 g (90% purity) of tert-butyl *N*-[2-[[[3-[4,4-bis(ethoxymethyl)cyclohexyl]-1*H*-pyrazol-4-yl]methyl](methyl)amino]ethyl]-*N*-methylcarbamate as a colorless oil. This reaction was repeated to give a total of 580 g (~90% purity) of product. This material (580 g, ~90% purity) was purified by reverse phase chromatography to provide tert-butyl *N*-[2-[[[3-[4,4-bis(ethoxymethyl)cyclohexyl]-1*H*-pyrazol-4-yl]methyl](methyl)amino]ethyl]-*N*-methylcarbamate (14, 318 g). C18 HPLC purity 99.3% (220 nm UV).

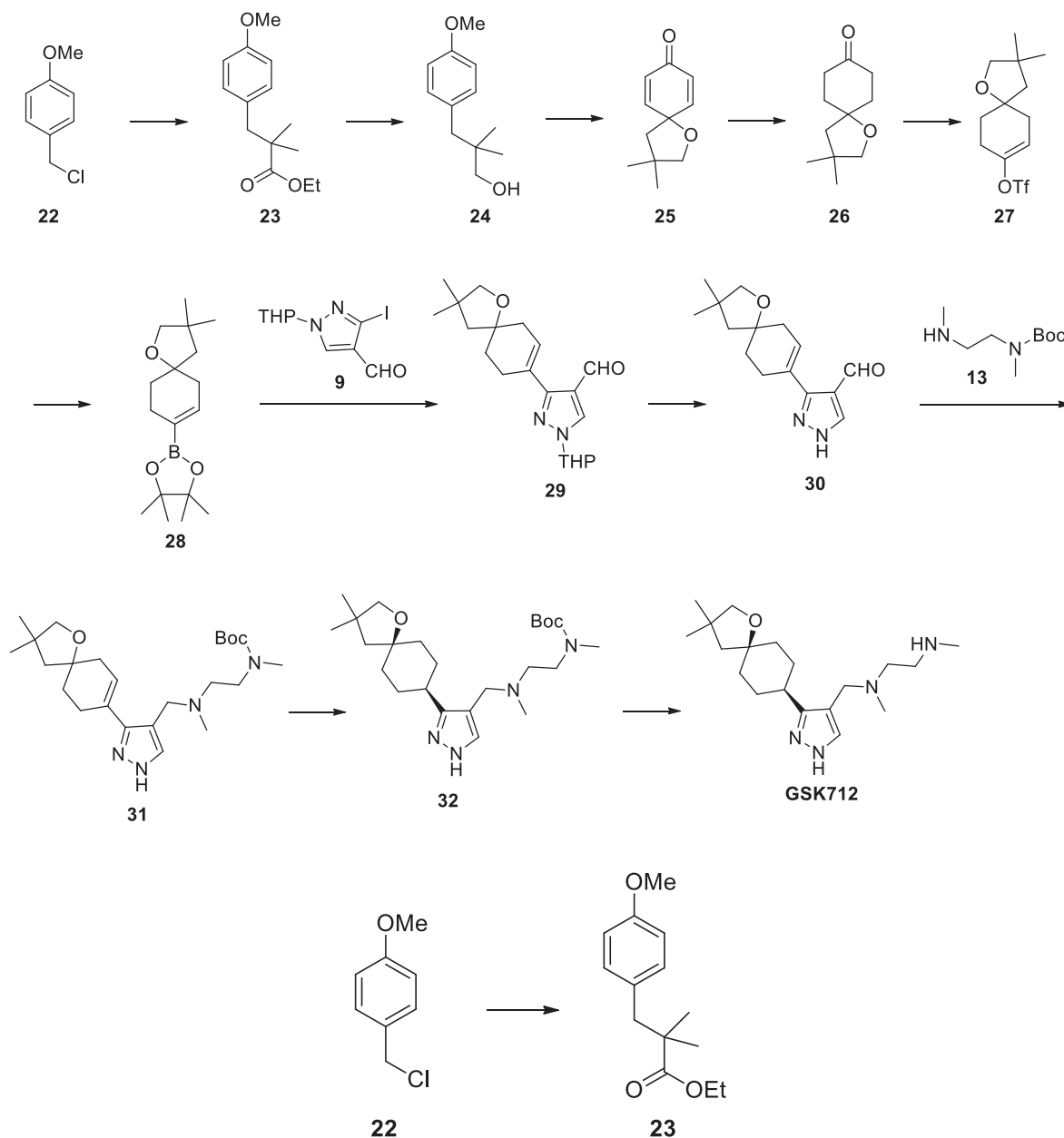


[2-[[[3-[4,4-bis(ethoxymethyl)cyclohexyl]-1*H*-pyrazol-4-yl]methyl](methyl)amino]ethyl](methyl)amine dihydrochloride (GSK715). HCl (gas) was introduced into a solution of tert-butyl *N*-[2-[[[3-[4,4-bis(ethoxymethyl)cyclohexyl]-1*H*-pyrazol-4-yl]methyl](methyl)amino]ethyl]-*N*-methylcarbamate (318 g, 681.44 mmol) in dichloromethane (2000 mL) with stirring until the HCl saturated the reaction solution at room temperature. The resulting solution was stirred for 4 h at room temperature. The resulting mixture was concentrated under vacuum. The residue was dissolved in 2 L of water. The pH value of the solution was adjusted to 11 with sodium hydroxide. The resulting solution was extracted with dichloromethane (4 x 2 L) and the organic layers were combined, dried over anhydrous sodium sulfate, filtered and concentrated under vacuum. The pure free base (207 g, 565.6 mmol) was dissolved in ethyl ether (2000 mL) and HCl (1.0M in ethyl ether, 1131 mL, 1131 mmol, 2.0 eq) was added dropwise with stirring. A solid began to form and clump up. The mixture was sonicated for 1 h to produce a free-flowing solid. The solid was collected by filtration and dried under high-vacuum to provide 231.2 g (77%) of [2-[[[3-[4,4-bis(ethoxymethyl)cyclohexyl]-1*H*-pyrazol-4-yl]methyl](methyl)amino]ethyl](methyl)amine dihydrochloride (GSK715 dihydrochloride) as a white solid. ¹H NMR (DMSO-*d*₆, 500MHz): δ (ppm) 9.27 (br s, 2H), 7.79 (s, 1H), 4.19-4.33 (m, 2H), 3.45-3.50 (m, 1H), 3.46 (br s, 1H), 3.43 (br s, 1H), 3.39-3.50 (m, 4H), 3.39-3.46 (m, 2H), 3.32 (br s, 1H), 3.15 (s, 2H), 2.80 (br t, *J*=11.6 Hz, 1H), 2.71 (s, 3H), 2.59 (br s, 3H), 1.63-1.73 (m, 2H), 1.57-1.63 (m, 2H), 1.56 (br s, 2H), 1.34-1.42 (m, 2H), 1.10-1.15 (m, 6H). ¹³C NMR (DMSO-*d*₆, 126MHz): δ (ppm) 151.2, 138.4, 105.3, 77.2, 69.8, 66.4, 66.4, 49.9, 49.5, 43.0, 38.7, 38.0, 33.4, 32.9, 29.7, 27.9, 15.5, 15.5. Elemental analysis for dihydrochloride (% calcd, % found for C₂₀H₄₀Cl₂N₄O₂ with 0.23 molar equiv of water by KF titration): C (54.10, 54.55), H (9.12, 9.74), N (12.62, 12.59). C18 HPLC purity 99.27% (220 nm UV).

¹H NMR Image of GSK715 (500 MHz, DMSO-d₆ + TFA)

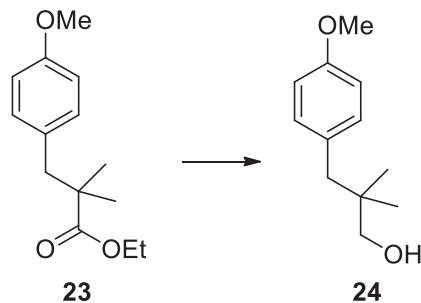
Synthesis of GSK3368712

Intermediates were characterized by LC-MS and/or ^1H NMR to confirm the structures and purity and carried to the next step without further purification unless otherwise noted. The synthetic scheme of GSK712 and preparation of indicated intermediates is described below.

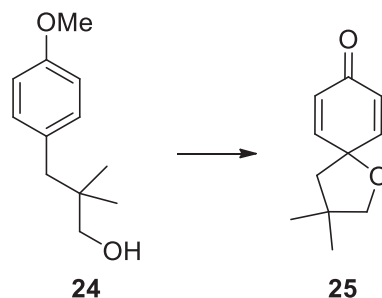


ethyl 3-(4-methoxyphenyl)-2,2-dimethylpropanoate (23). To a stirred solution of $i\text{Pr}_2\text{NH}$ (8.63 kg, 85 mol) in tetrahydrofuran (80 L) was added $n\text{-BuLi}$ (2.5 M in hexane, 34 L, 85 mol) dropwise at -78°C over 4 hours. The resulting solution was stirred for 2 hours at -45°C . To the reaction mixture was added ethyl 2-methylpropanoate (8.26 kg, 7.1 mol) dropwise with stirring at -78°C over 2 hours. The resulting solution was allowed for an additional 1 hour at -50°C . To the reaction mixture was added 1-(chloromethyl)-4-methoxybenzene (10 kg, 64 mol) dropwise with stirring at -78°C over 2 hours. The resulting solution was stirred for an additional 16 hours at room temperature. The reaction was then quenched by the addition of 3 L of saturated aqueous NH_4Cl solution. The resulting mixture was diluted with 3 L of H_2O and extracted with 3x10 L of ethyl acetate. The combined organic layers were

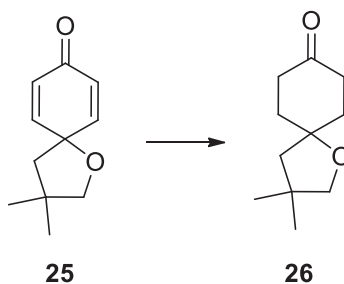
washed with brine (2 x 10 L), dried over anhydrous sodium sulfate, filtered and concentrated under vacuum. The residue was purified by silica gel chromatography eluting with petroleum ether/ethyl acetate (80:1 to 40:1) to provide 11 kg (65%) of ethyl 3-(4-methoxyphenyl)-2,2-dimethylpropanoate **23** as yellow oil. $^1\text{H NMR}$ (400 MHz, Chloroform-*d*) δ 7.03 (d, J = 8.8 Hz, 2H), 6.79 (d, J = 8 Hz, 2H), 4.11 (q, J = 7.2 Hz, 2H), 3.77 (s, 3H), 2.79 (s, 2H), 1.23 (t, J = 7.2 Hz, 3H), 1.15 (s, 6H).



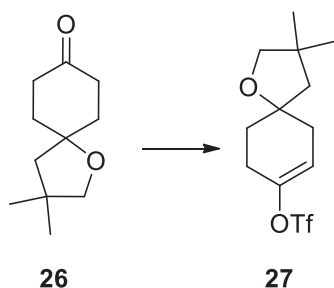
3-(4-methoxyphenyl)-2,2-dimethylpropan-1-ol (**24**). To a stirred solution of ethyl 3-(4-methoxyphenyl)-2,2-dimethylpropanoate (9 kg, 38 mol) in tetrahydrofuran (90 L) was added $\text{BH}_3\text{-Me}_2\text{S}$ (13 L, 129.7 mol) dropwise with stirring at -10°C . The reaction mixture was stirred for 16 hours at room temperature and quenched by the addition of 5 L of NH_4Cl solution. The resulting mixture was concentrated under vacuum, diluted with H_2O (10 L) and extracted with ethyl acetate (3 x 15 L). The combined organics were washed with brine (2 x 10 L), dried over sodium sulfate, filtered and concentrated under vacuum to give 5.9 kg (80%) of 3-(4-methoxyphenyl)-2,2-dimethylpropan-1-ol **24** as a white solid. $^1\text{H NMR}$ (400 MHz, DMSO-*d*6) δ 7.06 (d, J = 8.4 Hz, 2H), 6.82 (d, J = 8.8 Hz, 2H), 4.57 (t, J = 5.2 Hz, 1H), 3.72 (s, 3H), 3.07 (d, J = 5.2 Hz, 2H), 2.42 (s, 2H), 0.75 (s, 6H).



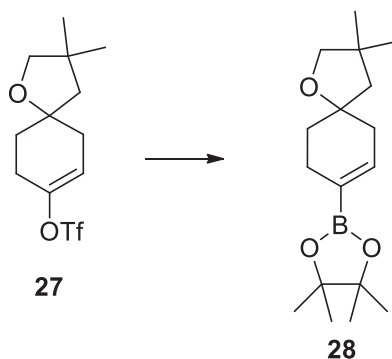
3,3-dimethyl-1-oxaspiro[4.5]deca-6,9-dien-8-one (**25**). To a cold (0°C) stirred solution of 3-(4-methoxyphenyl)-2,2-dimethylpropan-1-ol (5.7 kg, 29.4 mol) in AcCN (170 L) was added $\text{H}_4[\text{SiO}_4(\text{W}_3\text{O}_9)_4]\cdot x\text{H}_2\text{O}$ (22.8 kg) followed by [bis(trifluoroacetoxy)iodo]benzene (PIFA, 15.2 kg, 35.3 mol). The reaction mixture was stirred for 3 hours at 0°C , then quenched with 3% TEA-EtOAc (100 L) and the pH was adjusted to 8 with TEA. The resulting mixture was concentrated under vacuum and the crude residue was purified by silica gel chromatography, eluting with 1:50 EtOAc/PE to give 2.2 kg (42%) of 3,3-dimethyl-1-oxaspiro[4.5]deca-6,9-dien-8-one **25** as a yellow oil. $^1\text{H NMR}$ (400 MHz, Chloroform-*d*) δ 6.91 (d, J = 10.4 Hz, 2H), 6.11 (d, J = 10.0 Hz, 2H), 3.74 (s, 2H), 1.94 (s, 2H), 1.22 (s, 6H).



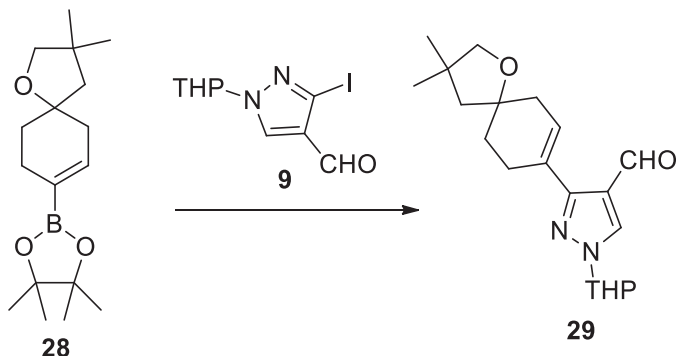
3,3-dimethyl-1-oxaspiro[4.5]decan-8-one (**26**). A mixture of 3,3-dimethyl-1-oxaspiro[4.5]deca-6,9-dien-8-one (2.5 kg, 14 mol) and palladium on carbon (400 g) in ethyl acetate (6 L) was stirred for 16 h at room temperature under 5 atm H_2 pressure. The solids were filtered out and the resulting filtrate was concentrated under vacuum. The residue was purified by silica gel chromatography eluting with ethyl acetate/petroleum ether (1:50) to provide 1.7 kg (66%) of 3,3-dimethyl-1-oxaspiro[4.5]decan-8-one **26** as a yellow oil. $^1\text{H NMR}$ (400 MHz, Chloroform-*d*) δ 3.58 (s, 2H), 2.73-2.65 (m, 2H), 2.27-2.21 (m, 2H), 2.21-2.09 (m, 2H), 1.87-1.80 (m, 2H), 1.67 (s, 2H), 1.14 (s, 6H).



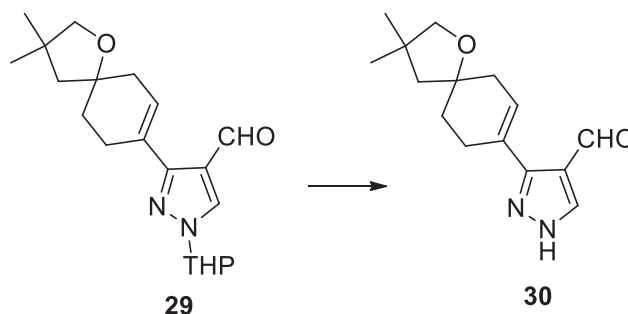
3,3-dimethyl-1-oxaspiro[4.5]dec-7-en-8-yl trifluoromethanesulfonate (27). To a cold (-78°C) stirred solution of 3,3-dimethyl-1-oxaspiro[4.5]decan-8-one (1.7 kg, 9.34 mol) in tetrahydrofuran (8.5 L) was added LiHMDS (1M in THF, 11.2 L, 11.2 mol) dropwise over 2 hours and the reaction mixture was stirred for an additional 1 hour at -78°C . 1,1,1-Trifluoro-N-phenyl-N-(trifluoromethane)sulfonylmethanesulfonamide (3.33 kg, 9.34 mol) was added and the resulting solution was stirred for 16 hours at room temperature. The reaction mixture was quenched by the addition of saturated aqueous NH_4Cl solution (5 L) and extracted with ethyl acetate (3 x 5 L). The combined organics were washed with brine (5 L), dried over anhydrous sodium sulfate, filtered and concentrated under vacuum. The crude residue was dissolved in ethane-1,2-diol (5 L) and extracted with hexane (2 x 10 L). The combined hexane layers were concentrated in vacuo to provide 2.2 kg (75%) of crude 3,3-dimethyl-1-oxaspiro[4.5]dec-7-en-8-yl trifluoromethanesulfonate 27 as a yellow oil. ^1H NMR (400 MHz, Chloroform-*d*) δ 5.64 (m, 1H), 3.56-3.51 (m, 2H), 2.61-2.58 (m, 1H), 2.56-2.27 (m, 3H), 1.96-1.91 (m, 1H), 1.81-1.74 (m, 1H), 1.68-1.60 (m, 2H), 1.13 (s, 6H).



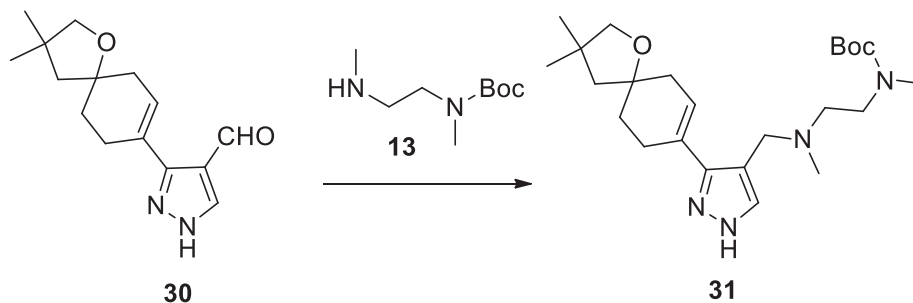
2-[3,3-dimethyl-1-oxaspiro[4.5]dec-7-en-8-yl]-4,4,5,5-tetramethyl-1,3,2-dioxaborolane (28). To a stirred solution of 3,3-dimethyl-1-oxaspiro[4.5]dec-7-en-8-yl trifluoromethanesulfonate (2.2 kg, 7 mol) in 1,4-dioxane (22 L), were added 4,4,5,5-tetramethyl-2-(tetramethyl-1,3,2-dioxaborolan-2-yl)-1,3,2-dioxaborolane (1.4 kg, 5.6 mol), KOAc (2.06 kg, 21 mol) and $\text{Pd}(\text{dppf})\text{Cl}_2$ (307.7 g, 0.42 mol) successively. The reaction mixture was stirred for 16 h at 80°C , then concentrated under vacuum. The crude residue was diluted with EtOAc (10 L) and washed with brine (2 x 5 L). The organic phase was dried over Na_2SO_4 , filtered and concentrated under reduce pressure. The residue was purified by silica gel chromatography eluting with ethyl acetate/petroleum ether (1:50) to provide 1400 g (68%) of 2-[3,3-dimethyl-1-oxaspiro[4.5]dec-7-en-8-yl]-4,4,5,5-tetramethyl-1,3,2-dioxaborolane 28 as a yellow oil. ^1H NMR (400 MHz, Chloroform-*d*) δ 6.46 (m, 1H), 3.52 (s, 2H), 2.36-2.13 (m, 4H), 1.74-1.7 (m, 1H), 1.64-1.55 (m, 3H), 1.26 (s, 12H), 1.11 (s, 6H).



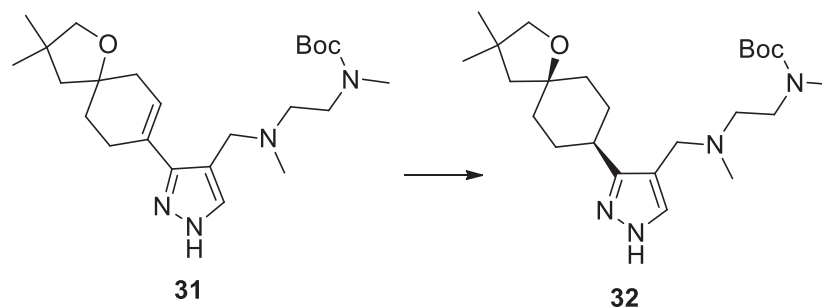
3-[3,3-dimethyl-1-oxaspiro[4.5]dec-7-en-8-yl]-1-(oxan-2-yl)-1*H*-pyrazole-4-carbaldehyde (29). A solution of 2-[3,3-dimethyl-1-oxaspiro[4.5]dec-7-en-8-yl]-4,4,5,5-tetramethyl-1,3,2-dioxaborolane (1.4 kg, 5.14 mol), 3-iodo-1-(oxan-2-yl)-1*H*-pyrazole-4-carbaldehyde (9, 1.32 kg, 4.64 mol), Pd(dppf)Cl₂ (366 g, 0.5 mol), Cs₂CO₃ (3.26 kg, 10 mol) and Cul (38 g, 0.4 mol) in 1,4-dioxane (14 L) and water (1.4 L) was stirred for 16 h at 120°C under nitrogen. The reaction mixture was allowed to cool to room temperature and concentrated under vacuum. The residue was diluted with EtOAc (10 L), washed with brine (2 x 3 L), and the organic phase was dried over Na₂SO₄, filtered and concentrated under reduced pressure. The residue was purified by silica gel chromatography eluting with ethyl acetate/petroleum ether (1:4) to provide 1120 g (70%) of 3-[3,3-dimethyl-1-oxaspiro[4.5]dec-7-en-8-yl]-1-(oxan-2-yl)-1*H*-pyrazole-4-carbaldehyde 29 as a yellow oil. ¹H NMR (400 MHz, Chloroform-*d*) δ 9.91 (s, 1H), 8.14 (s, 1H), 6.25-6.24 (m, 1H), 5.38-5.30 (m, 1H), 4.13-4.06 (m, 1H), 3.73-3.59 (m, 1H), 3.57-3.54 (m, 2H), 2.78-2.74 (m, 1H), 2.60-2.36 (m, 3H), 2.11-1.89 (m, 4H), 1.81-1.65 (m, 6H), 1.14 (s, 6H).



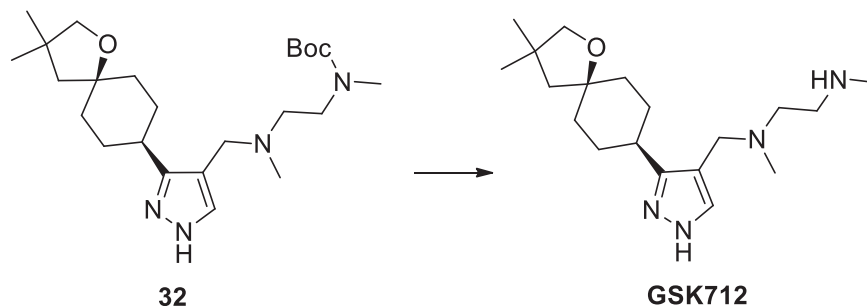
3-[3,3-dimethyl-1-oxaspiro[4.5]dec-7-en-8-yl]-1*H*-pyrazole-4-carbaldehyde (30). A mixture of 3-[3,3-dimethyl-1-oxaspiro[4.5]dec-7-en-8-yl]-1-(oxan-2-yl)-1*H*-pyrazole-4-carbaldehyde (1120 g, 3.25 mol) in methanol (4.4 L) and conc. hydrogen chloride (2.2 L) was stirred overnight (~16 hours) at room temperature. The resulting mixture was concentrated under vacuum and the resulting solution was diluted with 3 L of water. The pH of the solution was adjusted to 8 with aqueous sodium hydroxide (20%) and extracted with ethyl acetate (2 x 4 L). The combined organic layers were washed with brine (2 L), dried over anhydrous sodium sulfate, filtered and concentrated in vacuo. The residue was purified by silica gel chromatography eluting with ethyl acetate/petroleum ether (1:2) to provide 600 g (71%) of 3-[3,3-dimethyl-1-oxaspiro[4.5]dec-7-en-8-yl]-1*H*-pyrazole-4-carbaldehyde 30 as a yellow oil. LCMS(ES)+ *m/e* 261.1 [M+H]⁺. ¹H NMR (400 MHz, Chloroform-*d*) δ 9.92 (s, 1H), 8.04 (s, 1H), 6.31 (s, 1H), 3.59 (s, 2H), 2.75-2.73 (m, 1H), 2.54-2.39 (m, 3H), 2.05-1.98 (m, 1H), 1.85-1.80 (m, 1H), 1.75-1.65 (m, 2H), 1.16 (s, 6H).



tert-butyl *N*-(2-[[3-[3,3-dimethyl-1-oxaspiro[4.5]dec-7-en-8-yl]-1*H*-pyrazol-4-yl]methyl](methyl)amino)ethyl)-*N*-methylcarbamate (31). To a stirred solution of 3-[3,3-dimethyl-1-oxaspiro[4.5]dec-7-en-8-yl]-1*H*-pyrazole-4-carbaldehyde (600 g, 2.31 mol) in DCE (6 L) was added tert-butyl *N*-methyl-*N*-[2-(methylamino)ethyl]carbamate (13, 650 g, 3.46 mol) and the mixture was stirred at room temperature for 2 hours. NaBH(AcO)₃ (1.46 kg, 6.92 mol) was added and the resulting solution was stirred for 16 h at 70°C. The reaction mixture was then quenched by the addition of water (3 L) and extracted with dichloromethane (3 x 3 L). The combined organic layers were dried over anhydrous sodium sulfate, filtered and concentrated under reduced pressure. The residue was purified by silica gel chromatography eluting with dichloromethane/methanol (50:1) to provide 550 g (55%) of tert-butyl *N*-(2-[[3-[3,3-dimethyl-1-oxaspiro[4.5]dec-7-en-8-yl]-1*H*-pyrazol-4-yl]methyl](methyl)amino)ethyl)-*N*-methylcarbamate 31 as a yellow oil. [ANALYTICAL DATA]



Tert-butyl *N*-(2-[[[3-(3,3-dimethyl-1-oxaspiro[4.5]decan-8-yl)-1*H*-pyrazol-4-yl]methyl](methyl)amino]ethyl)-*N*-methylcarbamate (32). A mixture of tert-butyl *N*-(2-[[[3-(3,3-dimethyl-1-oxaspiro[4.5]dec-7-en-8-yl)-1*H*-pyrazol-4-yl]methyl](methyl)amino]ethyl)-*N*-methylcarbamate (550 g, 1.27 mol) in tetrahydrofuran and Pd(OH)₂ on carbon (165 g) was stirred for 16 h at room temperature under 5 atm of H₂ pressure. The solids were removed by filtration and the filtrate was concentrated under vacuum. The residue was purified by silica gel chromatography eluting with dichloromethane/methanol (50:1) to provide 550 g of the desired hydrogenated product as yellow oil. This material was purified by prep-chiral SFC [Column: CHIRALPAK AD-H SFC; Mobile Phase A: CO₂:60, Mobile Phase B: IPA (0.2% DEA):40] to provide 340 g of tert-butyl *N*-(2-[[[3-(3,3-dimethyl-1-oxaspiro[4.5]decan-8-yl)-1*H*-pyrazol-4-yl]methyl](methyl)amino]ethyl)-*N*-methylcarbamate 32 as a yellow oil. [ANALYTICAL DATA].



*N*1-((3-((5*S*,8*S*)-3,3-dimethyl-1-oxaspiro[4.5]decan-8-yl)-1*H*-pyrazol-4-yl)methyl)-*N*1,*N*2-dimethylethane-1,2-diamine (GSK712). A mixture tert-butyl *N*-methyl-*N*-(2-[methyl[[3-((5*S*,8*S*)-3,3-dimethyl-1-oxaspiro[4.5]decan-8-yl)-1*H*-pyrazol-4-yl]methyl)amino]ethyl) carbamate (340 g, 0.78 mol) in 5*N* HCl (gas)/DCM (3.4 L) was stirred for 5 h at room temperature. The resulting mixture was concentrated under vacuum and the residue was dissolved in distilled water (1.7 L) and the aqueous phase was treated with 100 g of activated carbon. The mixture was heated to 50°C for 1 hour, filtered, and the filtrate was basified to pH =12 with 4*N* NaOH at 0°C. The mixture was extracted with DCM (4 x 2 L) and the combined organic phase was dried over Na₂SO₄, filtered and concentrated. The residue was dissolved in CHCl₃ (2 L), 100 g of Silicycle thiol was added and the mixture was heated to 55°C for 3 hours. The mixture was filtered and the filtrate was concentrated in vacuo. The residue was dissolved in TBME (2 L) and then concentrated in vacuo, repeating this operation 3 times. The residue was crystallized from 1:2 TBME/heptane (2 L) to provide 190.7 g of crude material which was diluted with DCM and water. The pH of the aqueous layer was adjusted to 12 with 4 *N* NaOH at 0°C and the mixture was extracted with DCM (4 x 2 L). The combined organic phase was dried over Na₂SO₄, filtered and concentrated. The residue was crystallized from 1:2 TBME/heptane (1 L) to provide 168 g (64%) of *N*1-((3-((5*S*,8*S*)-3,3-dimethyl-1-oxaspiro[4.5]decan-8-yl)-1*H*-pyrazol-4-yl)methyl)-*N*1,*N*2-dimethylethane-1,2-diamine GSK712 as a white solid. LCMS(ES)⁺ *m/e* 335.2 [M+H]⁺. ¹H NMR (400 MHz, DMSO-*d*₆) δ 7.28 (br. s., 1H), 3.42 (s, 2H), 3.26 (s, 2H), 2.58-2.70 (m, 1H), 2.52-2.56 (m, 2H), 2.35 (t, *J*=6.34 Hz, 2H), 2.26 (s, 3H), 2.05 (s, 3H), 1.76-1.90 (m, 4H), 1.49-1.61 (m, 4H), 1.35-1.47 (m, 2H), 1.06 (s, 6H). ¹³C NMR (DMSO-*d*₆, 100 MHz): δ (ppm) 80.6, 77.6, 56.1, 53.0, 51.3, 49.2, 41.7, 37.1, 36.2, 28.5, 27.22. Elemental analysis (% calcd, % found for C₁₉H₃₄N₄O with 0.5 molar equiv of water: C (66.43, 66.03), H (10.27, 10.09), N (16.31, 16.18). C18 HPLC purity 97.9% (220 nm UV).

¹³C NMR Image of GSK712 (100 MHz, DMSO-d₆)

```

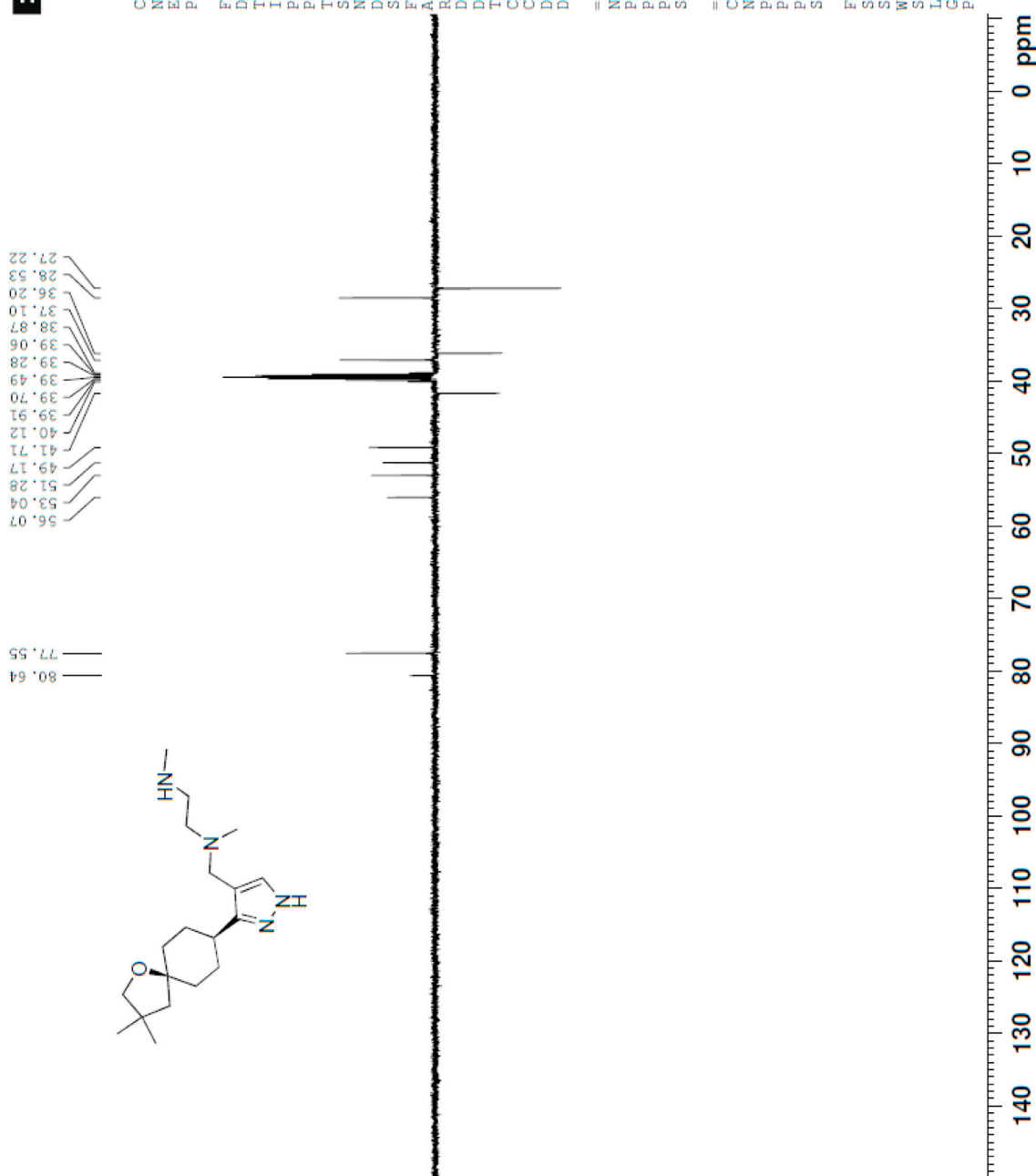
Current Data Parameters
NAME      GSK3368712B
EXPNO    10
PROCNO   1

F2 - Acquisition Parameters
Date_    20170113
Time     19.46
INSTRUM  spect
PROBHD   5 mm PABBO BB-
PULPROG  jmod
TD       65536
SOLVENT  DMSO
NS       256
DS       4
SWH      24038.461 Hz
FIDRES   0.366798 Hz
AQ       1.3631988 sec
RG       201.44
DC       20.800 usec
DE       6.50 usec
TE       297.1 K
CNST2    145.0000000
CNST11   1.0000000
D1       2.00000000 sec
D20      0.00689655 sec

===== CHANNEL f1 =====
NUC1     13C
P1       9.60 usec
P2       19.20 usec
PLW1     52.00000000 W
SFO1     100.6228298 MHz

===== CHANNEL f2 =====
CPDPRG2  waltz16
NUC2     1H
PCPD2    80.00 usec
PLW2     13.36600018 W
PLM12    0.44516999 W
SFO2     400.1316005 MHz

F2 - Processing parameters
SI       32768
SF       100.6128193 MHz
WDW      EM
SSB      0
LB       1.00 Hz
GB       0
PC       1.40
  
```



High Throughput Screen

Type I PRMT inhibitors were found through screening Epizyme's proprietary HMT-biased library (Mitchell et al., 2015). In summary, compound was incubated with PRMT1 for 30 minutes at room temperature (384-well plate) and reactions were initiated upon the addition of SAM and peptide. Final assay conditions were 0.75 nM PRMT1 (NP_001527.3, GST-PRMT1 amino acids 1-371), 200 nM 3H-SAM (American Radiolabeled Chemicals, specific activity 80 Ci/mmol), 1.5 μ M SAM (Sigma-Aldrich), and 20 nM peptide (Biotin-Ahx-RLARRGGVKRISGLI-NH₂, 21st Century Biochemicals) in 20 mM bicine (pH 7.6), 1 mM TCEP, 0.005% bovine skin gelatin, 0.002% Tween-20 and 2% DMSO. Reactions were quenched by the addition of SAM (400 μ M final). Terminated reactions were transferred to a Streptavidin-coated Flashplate (PerkinElmer), incubated for at least 1 hour and then the plate was washed with 0.1% Tween-20 using a Biotek ELx405 plate washer. The quantity of 3H-peptide bound to the Flashplate was measured using a PerkinElmer TopCount plate reader.

PRMT Biochemical Assays

All assays were performed with compound or DMSO prestamped (49x, 2% final) in 96 well plates (Costar, #3884). Assays for PRMT1 (NP_001527.3), PRMT3 (BPS, #51043), PRMT6 (BPS, #51049) and PRMT8 (NP_062828.3) used H4 1-21 peptide (AnaSpec, Inc. #AS-62499) and a buffer comprised of 50 mM Tris (pH 8), 0.002% Tween-20, 0.5 mM EDTA and 1 mM DTT. Briefly, Flag-his-tev-PRMT8 (61-394) was expressed in a baculovirus expression system and purified using Ni-NTA agarose affinity chromatography and Superdex 200 gel filtration chromatography. For all assays, final Adenosyl-L-Methionine (SAM) concentration listed contains a mixture of unlabeled SAM (NEB, #B9003S) and 3H-SAM (PerkinElmer NET155H001MC or NET155001MC). All reactions were quenched upon the addition of SAH (0.5 mM final).

For competition studies, substrate was added to the compound plate followed by the addition of enzyme. For SAM competition studies, final assay concentrations consisted of 2 nM PRMT1, 40 nM peptide and titrating SAM (50-8000 nM). For peptide competition studies, final assay concentrations consisted of 2 nM PRMT1, 1000 nM and titrating peptide (1.6-1000 nM). Reactions were incubated at room temperature for 18 minutes prior to quench.

For time dependence studies, enzyme/SAM mix was added to the compound plate and incubated for 3-60 minutes prior to addition of the peptide. For no preincubation assay, peptide was added to the compound plate followed by enzyme/SAM mix to initiate the reaction. Final PRMT1 assay concentrations were 0.5 nM PRMT1, 40 nM peptide and 1100 nM SAM. Reactions were incubated at room temperature for 20 minutes prior to quench.

For potency assessment against the PRMT family, enzyme/SAM mix was added to the compound plate and incubated for 60 minutes. Reactions were initiated upon the addition of peptide and quenched after 40 minutes. Final assay concentrations for PRMT1 consisted of 0.5 nM PRMT1, 40 nM peptide and 1100 nM SAM. PRMT3 assays contained 1 nM PRMT3, 160 nM peptide and 5800 nM SAM. PRMT6 and PRMT8 assays were comprised of 0.5 nM PRMT, 160 nM peptide and 1800 nM SAM. PRMT4 (BPS, #51047) assays consisted of 6 nM PRMT4, 400 nM rHistone H3.1 (NP_003520.1) and 400 nM SAM in 25 mM Tris (pH 8), 0.002% Tween-20, 0.5 mM EDTA, 200 mM NaCl and 2 mM DTT. PRMT5/MEP50 (NP_006100.2 and NP_077007.1, Chan-Penebre, et al) assays contained 4 nM PRMT5/MEP50, 50 nM H4 1-21 peptide and 980 nM SAM in 50 mM Tris (pH 8.5), 0.002% Tween-20, 4 mM MgCl₂ and 1 mM DTT. PRMT9 (NP_612373.2, Gerhart et al) assays contained 3 nM PRMT9, 150 nM SAP145 peptide (NSVPPVRHWCFKRKYLQGKRG -amide, 21st Century Biochemicals) and 3010 nM SAM in 25 mM Tris (pH 8), 0.002% Tween-20, 100 mM NaCl, 4 mM MgCl₂ and 1 mM DTT. PRMT7 assays consisted of 10 nM PRMT7 (Reaction Biology #HMT-21-382), 90 nM H2B peptide (AnaSpec #64385-1) and 2000 nM SAM in 50 mM Tris (pH 8), 0.002% Tween-20, 0.5 mM EDTA and 1 mM DTT. After quench, Arginine Binding Ysi SPA beads (PerkinElmer RPNQ0101, 1 mg/mL final) in 0.2M NH₄CO₃ were added to all assays excluding PRMT7, plates were sealed and equilibrated for \geq 30 min. Streptavidin SPA (PerkinElmer, RPNQ0007) beads were used for the PRMT7 assay. Plates were centrifuged and then read on a MicroBeta (PerkinElmer) following a \geq 200 min delay to measure the amount of tritium incorporated into the peptide substrate, reported as counts per minute (CPM).

Raw CPM values were converted to yield V_i/V_0 and analyzed using GraFit software. IC₅₀ values were determined using a 3-parameter model (Equation 1) where Background = fully inhibited value fixed to 0, Range = uninhibited value, [I] = concentration of inhibitor, IC₅₀ = half maximal inhibitory concentration and s = Hill Slope. For the competition studies, IC₅₀ data was fit to the Cheng-Prusoff equation for uncompetitive (Equation 2) or noncompetitive (Equation 3) inhibition where K_i = the binding affinity of the inhibitor, IC₅₀ = half maximal inhibitory concentration, [S] = the substrate concentration and K_m = the concentration of the substrate at which the enzyme activity is half maximal. K_i^{app} values were calculated based on the equation for an uncompetitive inhibitor and the assumption that the IC₅₀ determination was representative of the ESI* conformation. Additionally, the peptide competition data was fit to the formula for mixed inhibition (Equation 4) where CPM values were converted to CPM/minute and represent the velocity (v). K_i = the binding affinity of the inhibitor EI complex, K_i' = the binding affinity of the inhibitor ESI complex, V_{max} = maximal activity, [S] = the substrate concentration, [I] = the inhibitor concentration, and K_m = the concentration of the substrate at which the enzyme activity is half maximal. An alpha value ($\alpha = K_i'/K_i$) \neq 1 and >0.1 but <10 is indicative of a mixed type inhibitor.

$$V_i/V_0 = \text{Background} + \frac{\text{Range} - \text{Background}}{1 + \left(\frac{[I]}{IC_{50}}\right)^s} \quad (\text{Equation 1})$$

$$\text{If Uncompetitive; } K_i = \frac{IC_{50}}{1 + \left(\frac{K_m}{[S]}\right)} \quad (\text{Equation 2})$$

$$\text{If Noncompetitive; } K_i = IC_{50} \quad (\text{Equation 3})$$

$$v = \frac{V_{max} * [S]}{K_m \left(1 + \frac{[I]}{K_i}\right) + [S] \left(1 + \frac{[I]}{K_i'}\right)} \quad (\text{Equation 4})$$

Methyltransferase Biochemical Assays

In summary, methyltransferase was added to substrate solution and gently mixed. Substrate varied based on methyltransferase tested and was either nucleosome, core histones, histone H3, histone H4 or H3 1-21 peptide. Compound (10 μ M final) was added and incubated at room temperature for 10 minutes. Reaction was initiated upon the addition of 3H-SAM (1 μ M) and incubated for 1 hour at 30°C. Reaction mixture was delivered to P81 filter-paper and washed with PBS for detection via HotSpot proprietary technology. Data was analyzed using Excel.

In Cell Western

RKO cells were seeded in a clear bottom 384 well plates and treated with a 20-point two-fold dilution series of GSK3368715 (29,325.5 to 0.03 nM) or 0.15% DMSO. Plates were incubated for 3 days at 37°C in 5% CO₂. Cells were fixed with ice-cold methanol for 30 minutes at room temperature, washed with phosphate buffered saline (PBS), then incubated with Odyssey blocking buffer (Licor) for 1 hour at room temperature. Blocking buffer was removed and cells were incubated overnight at 4°C with rabbit anti-mono-methyl Arginine (MMA, Cell Signalling #8711 at 1:200) and mouse anti- α -tubulin (Sigma # T9026 at 1:5000) diluted in blocking buffer plus 0.1% Tween-20. Following PBS washes, secondary antibodies IRDye 800CW goat anti-Rabbit IgG (H+L) and IRDye 680RD goat anti-mouse IgG (H+L) (Li-cor # 926-32211 and 926-68070) were applied for 1 hour. Plates were washed thoroughly with PBS, then ddH₂O and allowed to dry at room temperature. Plates were scanned and analyzed using the Li-Cor Odyssey imager and software. The relative MMA expression was determined by dividing the integrated intensity of MMA by the integrated intensity of tubulin using Microsoft Excel. The MMA level was then plotted against the log concentration of the compound and plotted using a 4-parameter fit equation using GraphPad Prism 6.0.

Western Blots

Cells were seeded in 6 well plates in 2 to 4 mL of cell culture media. Plates were dosed on 24 hours after seeding with 2 μ M GSK3368715 or 0.15% DMSO. Cell pellets were collected at 3, 6, 24, 48, 72, 96, 120, 144, and 168 hours post dosing. Cell pellets were lysed in 4% SDS and homogenized by QIAshredder column (QIAGEN), and protein concentrations determined by BCA Protein Assay (Pierce). Gel loading samples were denatured in NuPAGE LDS Sample Buffer and Sample Reducing Agent (Life Technologies) and loaded onto NuPAGE Novex 4-12% Bis-Tris gels, (Life Technologies) resolved using MES running buffer and transferred onto nitrocellulose membrane (Life Technologies) using IBlot2 (Life Technologies). Blots were blocked in blocking buffer (Li-Cor), followed by incubation with either tubulin (Sigma #T9026 at 1:10,000), MMA (Cell Signaling #8711 at 1:2,000), SDMA (Cell Signaling 13222S, clone D2C3D6, 1:1000), or ADMA (Cell Signaling #13522S at 1:250) diluted in blocking buffer plus 0.1% Tween-20 overnight at 4°C. Blots were washed thoroughly in PBST (Cell Signalling #9809) and secondary antibodies (IRDye, Li-Cor) were applied with incubation at room temperature for 1 hr at 1:10,000. Blots were scanned and analyzed using Li-Cor Odyssey imager and software.

Cell Proliferation Assay

Growth inhibition in response to GSK3368712 and GSK3368715 was evaluated as previously described (McCabe et al., 2012). Data were fit with a four-parameter equation to generate a concentration response curve. The growth IC₅₀ (gIC₅₀) and growth IC₁₀₀ (gIC₁₀₀) are the points at which 50% and 100% inhibition of growth are achieved, respectively. Growth Inhibition is the percent maximal inhibition and was calculated as $100 - ((y_{min} - 100) / (y_{max} - 100) * 100)$. Y_{min}-T₀ values were calculated by subtracting the T₀ value (100%) from the y_{min} value on the curve, and are a measure of net population cell growth or death. Growth Death Index (GDI) is a composite representation of Y_{min}-T₀ and percent maximal inhibition. If Y_{min}-T₀ values are negative, then GDI equals Y_{min}-T₀; otherwise, GDI represents the fraction of cells remaining relative to DMSO control (y_{max}) and (y_{min}): $(y_{min} - 100) / (y_{max} - 100) * 100$. A minimum of two biological replicates were evaluated for each assay.

Evaluation of Synergistic Effects on Cell Proliferation

A double titration of GSK3368715 (or GSK3368712) and GSK3203591 was performed for 6 days as described above, except that cells were dosed with a 16-pt, 2-fold dilution matrix of both agents, ranging in concentration from 0.3 to 10,000 nM. Single agent titrations were run in parallel. Bliss independence analysis was performed using growth inhibition value for each combination and a synergy score determined as previously described (McGrath et al., 2016).

Cell Cycle Analysis

The Toledo or OCI-Ly1 DLBCL cell lines were treated with a 5-point, 10-fold dilution series GSK3368715 or 0.1% DMSO for 10 days. On days 3, 5, 7, and 10 cell nuclei were isolated and DNA was stained with propidium iodide using CycleTEST PLUS DNA Reagent Kit (Becton Dickinson) per the manufacturer's instructions. Fluorescence was measured using a Becton Dickinson FACS Calibur flow cytometer. Cell cycle phase distribution was determined by the Watson Pragmatic mathematical model using FlowJo software.

Caspase 3/7 Assay

The effect of GSK3368715 treatment on cellular caspase-3/7 activity was measured with Caspase-Glo™3/7 assay kit (Promega). Assays were performed according to the manufacturer's instructions. Cells were plated and dosed with GSK3368715 or DMSO as described for the cell proliferation assay. At each timepoint, CellTiter-Glo reagent was added to duplicate plates to assess cell viability and Caspase-Glo 3/7 reagent was added to another pair of duplicate plates to assess cell death. The luminescence signal was measured with an EnVision Plate Reader (Perkin Elmer). Caspase 3/7 Glo and CTG values for GSK3368715 and DMSO were background subtracted for each plate. To account for cell number, Caspase 3/7 Glo values for each dose were then normalized to their corresponding CTG value. Normalized Caspase 3/7 Glo values were expressed as a fold increase over the average DMSO Caspase 3/7 Glo value for each dose of GSK3368715. Fold-increases for replicate plates were then averaged for each biological replicate.

RNA-seq and Differential Splicing Analysis

RNA samples were converted into cDNA libraries using the Illumina TruSeq Stranded mRNA sample preparation kit (Illumina). Samples were sequenced at a depth of 100 million paired-end reads per sample, 100base-pair read length. QC of the Fastq files was performed using FastQC (<https://www.bioinformatics.babraham.ac.uk/projects/fastqc/>) (Andrews, 2010) and aligned to GRCh38 version 23 downloaded from Ensembl using STAR v2.5.2b (Dobin et al., 2013). The BAM files obtained from STAR were filtered, sorted, and indexed using RSeQC (<http://rseqc.sourceforge.net/>) (Wang et al., 2012, 2016) and SAMtools (<http://www.htslib.org/>) (Li et al., 2009). rMATS was used to identify differential alternative splicing events from the relevant BAM files. Average reads per million (RPM) were computed for each event by averaging the RPM value for each condition involved in the rMATS comparison. A cutoff of 0.5 average RPM was used to filter out low expressing events. A cutoff of 5% ΔEIL and an adjusted p value cutoff of 1% was used to identify significant differentially spliced events. Custom R scripts were used to implement all these cutoffs for all the comparisons. Heatmaps were generated in R using the “gplots” and “RColorBrewer” package found in Bioconductor. Size-proportional overlaps were generated using the online tool BioVenn (<http://www.biovenn.nl/>) (Hulsens et al., 2008).

Splicing Validation

Selected skipped exon events were confirmed using qRT-PCR. Reverse transcription (RT) was carried out using a High capacity cDNA kit (Applied Biosystems) following manufacturer's instructions, from the RNA samples used for RNA-seq. RT reactions took place in PCR blocks set at 25°C for 10 min, 37°C for 2 hours, 85°C for 10 min, then 4°C until analysis. Taqman qRT-PCR was carried out using Fast taq man master mix (Applied Biosystems) and triplicate PCR reactions were run on ABI ViiA 7 (Applied Biosystems) according to the manufacturer's protocol. Taqman probes (Applied Biosystems) for splicing events were chosen to cover the upstream exon, downstream exon, the skipped exon, and a constitutive exon. The constitutive taqman probe was normalized using housekeeper genes, *GAPDH* and *ACTB*. The upstream, downstream, and skipped taqman probes were normalized to the constitutive exon and the average $2^{-\Delta\Delta CT}$ values were calculated. The frequencies of the fold change from control of qRT-PCR was compared to fold change from control from the RNA-seq data using a chi-square test and p values less than 0.05 was considered a validated skipped exon event, p value equal to or greater than 0.05 and less than 0.1 were called questionable, and p values more than 0.01 were considered not validated.

Identification of Proteins with Arginine Methylation Changes

Cell lines were cultured with 0.1% DMSO, 2 μM GSK3368712, 0.5 μM GSK3203591, or a combination of GSK3368712 & GSK3203591 for 4 days. Cells were collected in freshly prepared lysis buffer (20 mM HEPES, pH 8.0; 9.0 M Urea; 1 mM sodium orthovanadate, activated; 2.5 mM sodium pyrophosphate; 1 mM β-glycerol-phosphate) and flash frozen. Cellular extracts prepared in urea lysis buffer were reduced, alkylated and digested with trypsin. 45 mg total protein for each sample was desalted over SEP PAK C18 columns and split into 3-15 mg aliquots for enrichment with the Mono-Methyl Arginine Motif Antibody (#12235), Asymmetric Di-Methyl Arginine Motif Antibody (#13474), and Symmetric Di-Methyl Arginine Motif Antibody (#13563). Enriched peptides were purified over C18 STAGE tips, subjected to secondary digest with trypsin and re-purified over STAGE tip prior to LC-MS/MS analysis. Two non-sequential replicates were run for each enrichment. Proteomic analysis was carried out using the MethylScan method as previously described (Guo et al., 2014).

Each enriched sample was analyzed by liquid chromatography-tandem mass spectra (LC-MS/MS) in a data-dependent manner on either a Thermo Orbitrap Q Exactive or Fusion Lumos Tribrid mass spectrometer using a top-twenty MS/MS method with a dynamic repeat count of one, and a repeat duration of 30 sec. Peptides were eluted using a 120-minute linear gradient of acetonitrile in 0.125% formic acid delivered at 280 nL/min. Peptide sequences were identified by searching MS/MS spectra against the SwissProt *Homo sapiens* database using SEQUEST (Eng et al., 1994) with a mass accuracy of 5 ppm for precursor ions and 0.02 Da for product ions. Enzyme specificity was set to semi-trypsin with up to four mis-cleavages allowed. Cysteine carboxamidomethylation was specified as a fixed modification, oxidation of methionine and mono- or di-methylation on arginine residues were allowed as variable modifications. Reverse decoy databases were included for all searches to estimate false discovery rates, and filtered using a 2.5% FDR. All quantitative results were generated using Skyline (MacLean et al., 2010) to extract the integrated peak area of the corresponding peptide assignments. Accuracy of quantitative data was ensured by manual review in Skyline or in the ion chromatogram files.

Since the presence of a dimethylated arginine may inhibit the activity of trypsin at that site (Brostoff and Eylar, 1971), changes to ADMA and SDMA could result in a differential pattern of tryptic digestion, and manifest as an apparent increase in arginine methylation. Nonetheless, the appearance of distinct trypsin cleavage products could reflect a change in the methylation state at an arginine residue allowing for identification of proteins that show arginine methylation changes in response GSK3368712.

Fold changes were calculated for each treatment relative to the DMSO control. Fold change between immunoprecipitations replicates of each condition were calculated as a measure of variance. For each comparison, we required: 1) the fold change observed between two conditions to be at least 1.5 fold greater than the sum of the fold changes between the replicates of the two conditions; 2) methylated peptides identified in more than one sample; 3) the presence of at least one instance of monomethyl mark (for MMA immunoprecipitations) or dimethyl mark (for ADMA or SDMA immunoprecipitations) on the detected peptide.

Custom R scripts, using the “dplyr” package found in Bioconductor, were used to generate lists of proteins meeting all these cut-offs for all the comparisons and methyl-marks. In a given cell line, protein lists were merged for all 3 methyl marks and duplicates were removed to obtain a master list of proteins with a change in any methyl mark. Overlaps were generated using BioVenn (<http://www.biovenn.nl/>) to obtain a list of changed proteins, common across cell lines and tumor types. A hypergeometric test of over-enrichment was performed using the Molecular Signatures Database webtool for overlap enrichment on the list of gene names of the common proteins using the Hallmark (H) and Reactome (CP) gene sets. Heatmaps were generated in R using the “gplots” and “RColorBrewer” package found in Bioconductor. Scatterplots were generated in R using the “ggplot2” package found in Bioconductor.

Identification and Quantitation of Dimethylated Arginines in KHRBS1 by LC-MS/MS Analysis

Panc03.27 cells were cultured with 0.1% DMSO, 2 μ M GSK3368712, 0.5 μ M GSK3203591, or a combination of GSK3368712 & GSK3203591 for 4 days, collected, and lysed in RIPA buffer (Sigma). KHRBS1 was immunoprecipitated with Rabbit anti-KHRBS1 antibodies (Bethyl) using the Pierce Classic Magnetic IP/Co-IP Kit (Pierce) per manufacturer instructions. Immunoprecipitated eluates were separated by SDS-PAGE and visualized by Coomassie staining. The KHRBS1 band were excised, reduced and alkylated, and digested overnight with trypsin (Promega). After organic extraction, samples were injected on an Easy nLC1000 UHPLC system (Thermo Scientific). The nanoLC was interfaced to a Q- Exactive Hybrid Quadrupole-Orbitrap Mass Spectrometer (Thermo Scientific). Tryptic peptides were separated on a 25 cm x 75 μ m ID, PepMap C18, 3 μ m particle column (Thermo Scientific) using a 40 min gradient of 2-30% acetonitrile/0.2% formic acid and a flow of 300 nL/min. MS-based peptide sequencing was accomplished by tandem mass spectrometry using data dependent LC-MS/MS. Uninterpreted tandem MS spectra were searched for peptide matches against the human UniProt protein sequence database using Mascot (Matrix Science). Carbamidomethylation was selected as a fixed modification on Cys residues. Oxidation on Met and methylation and dimethylation on Arg residues were selected as variable modifications. MS/MS spectra for methylated peptides were manually validated to confirm the site of mono or dimethylation. Integrated peak areas from Extracted Ion Chromatograms (XICs) from the MS scan were used for the relative quantitation of un-, mono- and dimethylation in control and inhibitor treated samples. Identified KHRBS1 methylation sites were further interrogated using a parallel reaction monitoring (PRM) method targeting the dimethylated peptides. Diagnostic ions for either ADMA (neutral loss of 45.0578) or SDMA (neutral loss of 31.0422) were monitored and allowed the determination of the ADMA/SDMA for each arginine dimethylation site.

Determination of Intracellular MTA Levels

Confluent cells were washed with fresh media, scraped in a 1:1 ratio of media and 0.1% formic acid, and mixed with acetonitrile. Samples were stored at -80°C until analysis. A separate well was trypsinized and counted using a ViCell (Beckman) for both cell number and average diameter, which was used to calculate intracellular volume. Absolute MTA levels in each sample were determined from a standard curve of MTA, by LC/MS/MS on a Triple Quadrupole Mass Spectrometer (AB Sciex Instruments) with an Acuity UPLC HSS column. Intracellular MTA levels were calculated by dividing the μ mol of MTA per cell number by the cell volume.

QUANTIFICATION AND STATISTICAL ANALYSIS

Statistical analyses were performed using Microsoft Excel or GraphPad Prism (Version 7.02). Sample sizes are indicated in the figure legends and data are expressed as the mean \pm standard error of the mean (SEM) or standard deviation (SD) as indicated in the figure legends and methods. Statistical significance was evaluated using a two-tailed Student's *t*-test.

DATA AND SOFTWARE AVAILABILITY

Raw RNA-seq data were deposited into the National Center for Biotechnology Information (NCBI)'s Gene Expression Omnibus, GEO: GSE126651. The mass spectrometry proteomics data have been deposited to the ProteomeXchange Consortium via the PRIDE partner repository, PRIDE: PXD012747. X-ray crystallography coordinates were deposited in Protein Data Bank, PDB: 6NT2.